ACSNANO

www.acsnano.org

ARTICLE

Molecular Conformation of Bent-Core Molecules Affected by Chiral Side Chains Dictates Polymorphism and Chirality in Organic Nano- and Microfilaments

Jiao Liu, Sasan Shadpour, Marianne E. Prévôt, Michael Chirgwin, Ahlam Nemati, Elda Hegmann, Robert P. Lemieux, and Torsten Hegmann*

Cite This: *ACS Nano* 2021, 15, 7249–7270

Read Online

ACCESS | Metrics & More | Article Recommendations | Supporting Information

ABSTRACT: The coupling between molecular conformation and chirality is a cornerstone in the construction of supramolecular helical structures of small molecules across various length scales. Inspired by biological systems, conformational preselection and control in artificial helical molecules, polymers, and aggregates has guided various applications in optics, photonics, and chiral sorting among others, which are frequently based on an inherent chirality amplification through processes such as templating and self-assembly. The so-called B4 nano- or microfilament phase formed by some bent-shaped molecules is an exemplary case for such chirality amplification across length scales, best illustrated by the formation of distinct nano- or microscopic chiral morphologies controlled by molecular conformation. Introduction of one or more chiral centers in the aliphatic side chains led to the discovery of homochiral helical nanofilament, helical microfilament, and heliconical-layered nanocylinder morphologies. Herein, we demonstrate how *a priori* calculations of the molecular conformation affected by chiral side chains are used to design bent-shaped molecules that self-assemble into chiral nano- and microfilament as well as nanocylinder conglomerates despite the homochiral nature of the molecules. Furthermore, relocation of the chiral center leads to formation of helical as well as flat nanoribbons. Self-consistent data sets from polarized optical as well as scanning and transmission electron microscopy, thin-film and solution circular dichroism spectropolarimetry, and synchrotron-based X-ray diffraction experiments support the progressive and predictable change in morphology controlled by structural changes in the chiral side chains. The formation of these morphologies is discussed in light of the diminishing effects of molecular chirality as the chain length increases or as the chiral center is moved away from the core-chain juncture. The type of phase (B1-columnar or B4) and morphology of the nano- or microfilaments generated can further be controlled by sample treatment conditions such as by the cooling rate from the isotropic melt or by the presence of an organic solvent in the ensuing colloidal dispersions. We show that these nanoscale morphologies can then organize into a wealth of two- and three-dimensional shapes and structures ranging from flower blossoms to fiber mats formed by intersecting flat nanoribbons.

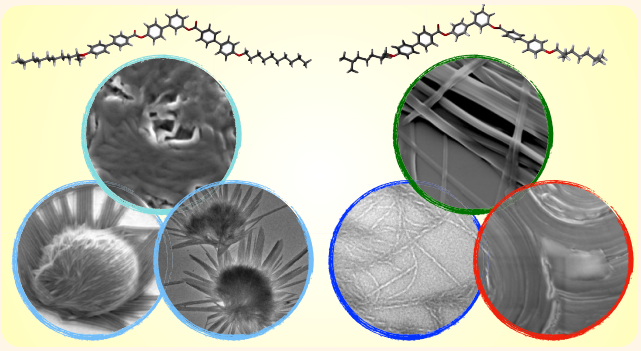

KEYWORDS: *organic helical nano- and microfilaments, molecular conformation, self-assembly, polymorphism, chirality, bent-core liquid crystals, B4 phase*

Helical structures and shapes are formed by a cornucopia of physical and biological systems, either engineered or formed spontaneously at length scales from the subnm regime to macroscopic objects.[1−5] Like most of the biologically active molecules such as proteins, sugars, and nucleic acids,[6−11] man-made organic,[12] inorganic[13−17] and hybrid materials[18,19] can be designed to assemble into helical

Received: January 19, 2021
Accepted: March 15, 2021
Published: March 18, 2021

https://doi.org/10.1021/acsnano.1c00527
ACS Nano 2021, 15, 7249–7270

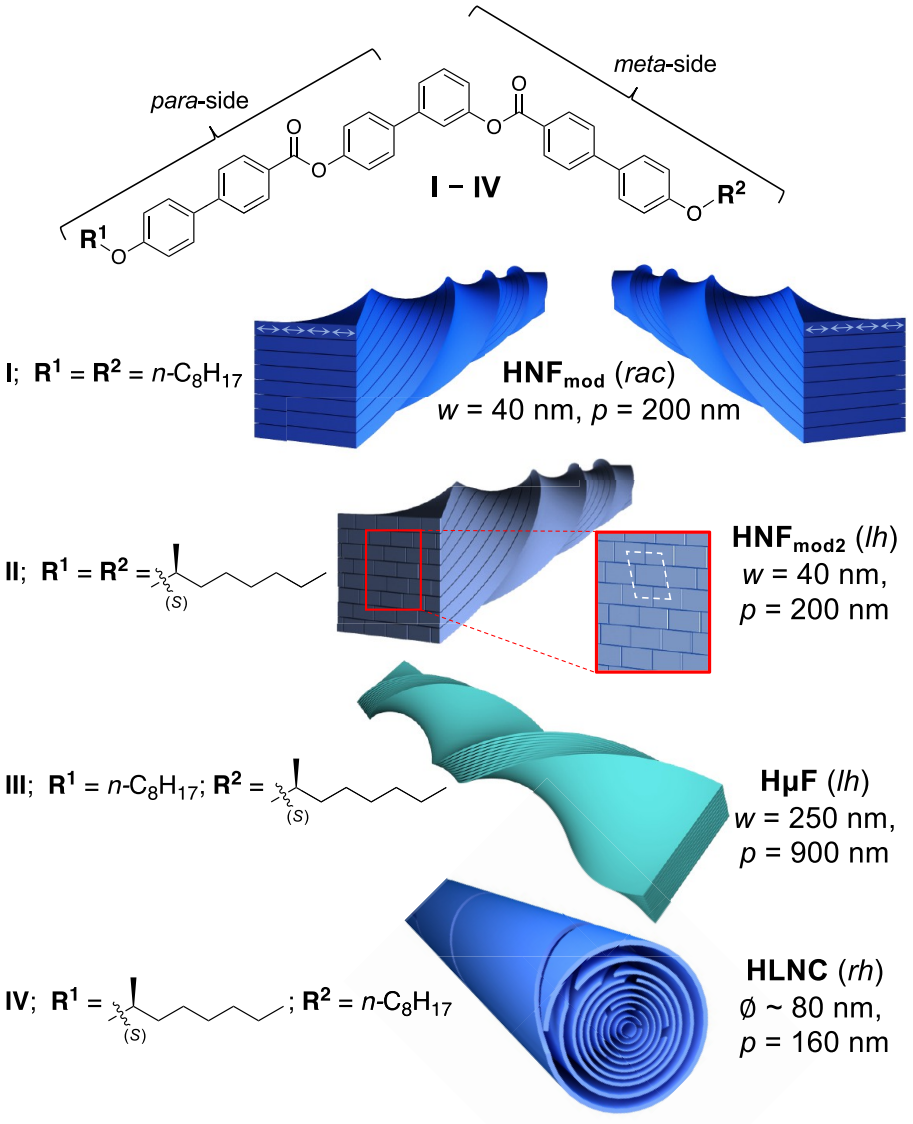

Figure 1. Tris-biphenyl-based bent-core materials I–IV[76,77,79] forming a range of possible B4 morphologies depending on the presence or absence of a chiral center at C-1 in both aliphatic side chains and the side chain of either the longer *para*-side or the shorter *meta*-side of the molecule. The experimentally observed handedness depends on the configuration of the chiral center(s) for II–IV, the conglomerate with equal proportions of heterochiral domains as formed by I, and the dimensions of each morphology are given. Double-sided arrows in the HNF_{mod} morphology indicate the intralayer modulation; the white parallelogram in the HNF_{mod2} morphology indicates both the intra- and interlayer modulations.

nanoscale morphologies.[20−26] The underlying mechanisms driving these assembly processes take advantage of chirality transfer across length scales[27,28] from the molecular or nanoscale to the supramolecular, even the macroscopic level,[27,29,30] through a range of intermolecular forces and sergeant-soldier[31,32] or majority-rules effects[33,34] among others. Furthermore, other approaches utilize chiral templates[35] or molecular changes affecting the conformation or shape of molecules and nanostructures to spontaneously promote helical structure formation. Examples range from inorganic subnm nanowires[36] and nanocrystals[37−40] over polymers[41−45] and polymer networks[46] to amphiphiles, surfactants,[47] and a considerable variety of other organic,[12] inorganic,[48−50] and organometallic molecules.[51,52]

Without delving into the details of molecular parity violations and their role in biomolecular homochirality,[53] the absence of any chiral bias, especially the absence of molecular chirality,[54] results in the formation equal proportions of left- and right-handed molecules or helical (super)structures no matter what the underlying driving force,[55] unless there is an energetic imbalance that gives rise to symmetry breaking.[56] Prime examples supporting this argument in the field of soft condensed matter are phases formed by molecules with a pronounced bent molecular shape. Such bent-core molecules can form an assortment of phases including the heliconical twist-bend nematic (N_{TB})[57−64] and the twist-bend smectic (SmC_{TB}) phase[65] as well as layered structures of so-called dark conglomerate (DC) or sponge phases,[66,67] a rather short pitch (~14 nm) helical ferroelectric tilted smectic phase ($SmC_SP_F^{hel}$),[68] and B4 filament-type phases.[54,69−72] Morphological variations of the latter (morphology, from the Greek root *morpho-*, meaning shape, and defined as the study of shape) now include helical nano- and microfilaments with varying dimensions (width, pitch) as well as in- or interlayer

https://doi.org/10.1021/acsnano.1c00527
ACS Nano 2021, 15, 7249−7270

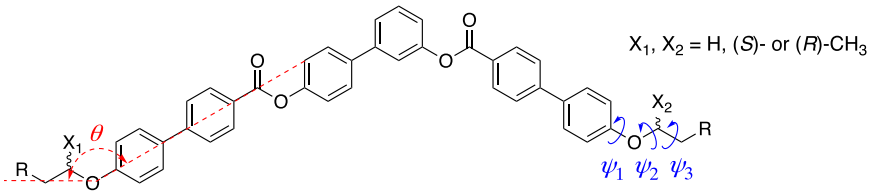

Figure 2. Conformational analysis: (a) Previously analyzed dihedral angle distributions at the core-chain juncture around the first three single bonds indicated by ψ_1–ψ_3 and bend angle at the core-chain juncture θ.[79]

modulation,[54,73–77] heliconical nanocrystallites,[78] and finally heliconical-layered nanocylinders.[79] Practically all these filament- and nanocylinder-based B4 phase morphologies were realized by strategically incorporating chiral centers into the aliphatic side chains of bent-core molecules featuring up to three biphenyl segments (Figure 1).[74,76,77,79] Furthermore, all B4 nano- and microscale morphologies display a characteristic blue structural color (in reflection mode),[80,81] whose origin is not entirely understood but certainly linked to diffraction, scattering, or interference *via* the periodic nano- to microscale layering and packing of these filaments in thin films.[82]

Single molecule stochastic dynamics (SD) atomistic simulations revealed that the position of the chiral center at the core-chain junction of these bent-core molecules either in the shorter *meta*- or the longer *para*-side of these asymmetric bent-shaped molecules imparted significant changes in the core-chain angle distributions as well as in the dihedral distribution functions of the first three bonds in the aliphatic side chain ψ_1–ψ_3 (Figure 2).[79] When the chiral center resides in the longer *para*-side, such as in compound **IV**, a significant shift to lower bend angles is observed at the core-chain junction (Figure 2) in comparison to the bend angle θ calculated for molecule **III** where the chiral center is situated in the shorter *meta*-side. Furthermore, the chiral center in the *para* side chain of **IV** changes the local topology of the connection of the alkoxy chain to the molecular core, subsequently leading to more opportunities for twisted conformations than when the chiral center is situated in the *meta* side chain as in compound **III**. These changes in conformational distributions as a result of the placement of chiral centers in the *para*- or *meta*-sides then affect the average molecular dimensions with a lower average aspect ratio for **IV** in comparison to **III**. The sum of these conformational differences governs the type of curvature of these B4 layer structures with saddle splay deformations for the microfilaments formed by **III** (HμF), here exclusively upon rapid cooling, and cylindrical (zero Gaussian) curvature in the heliconical-layered nanocylinders (HLNC) formed by **IV**.[79] With chiral centers in each side chain, the conformation of the entire molecule then results in helical filaments with lower overall dimensions and additional in-layer for compound **I** (HNF_{mod}) and in-layer as well as interlayer modulations for **II** (HNF_{mod2}), respectively (Figure 1).[74,77]

By establishing a link between the B4 morphology and the lowest-energy conformation affected by the distribution of dihedral angles in the core-chain junctions,[79] the next logical question was how the position of the chiral center in and the length of the aliphatic side chain[73] affect curvature and thereby, as documented, the formation of the various B4 morphologies. Moreover, these changes in the aliphatic side chains affect the observed polymorphism between the B1 and B4 phases as well as the biphasic behavior observed for these bent-core molecules.

Consequences for the helical pitch, the magnitude of the spontaneous polarization, and the phase stability, respectively, impacted by the position and configuration of chiral centers have essentially been studied for all chiral liquid crystalline phases such as chiral nematic (N*), chiral smectic-C (SmC*), other tilted chiral smectic as well as twist-grain boundary (TGB*) and blue phases (BP*). From an abundance of experimental studies on these chiral phases, two general trends emerged and were reviewed by Goodby *et al.* and others.[83,84] The key findings were the following: First, increasing the length of terminal aliphatic chains appended to a chiral center positioned at the core-chain juncture diminishes the effects of chirality with increasing chain length. The chiral center is described as increasingly buried in the overall structure, thereby diluting the effect of the chiral center by increasing the relative size (volume) of the aliphatic molecular substructure, especially in smectic layers. Second, and analogously, moving the chiral center away from the core-chain juncture reduces any restraint of rotation about the chiral center that effectively reduces the effects of chirality in the side chain.[83]

To analyze the consequences of introducing longer chiral side chains when the chiral center remains at C1 as well as relocating the chiral center away from the core-chain juncture to C2, we synthesized and characterized two structurally correlated sets of tris-biphenyl-based bent-core compounds **1**–**5** (Figure 3). Compounds **1** and **2** feature (*S*)-2-decyloxy side chains, which extend the length by two methylene groups in

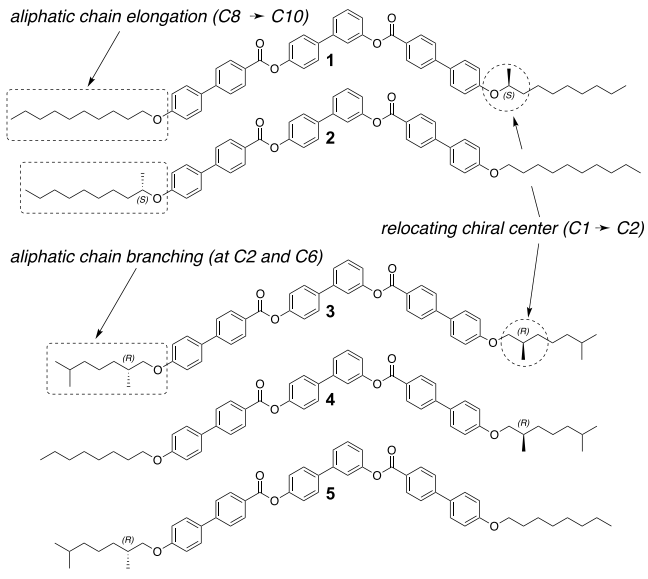

Figure 3. Bent-core compounds with either (*S*)-2decyloxy- (1, 2) or (*R*)-2,6-dimethylheptyloxy side chain(s) (3–5) in both or either the longer *para*- or the shorter *meta*-side of the molecule; changes with respect to the parent molecules I–IV (Figure 1) are indicated.

https://doi.org/10.1021/acsnano.1c00527
ACS Nano 2021, 15, 7249–7270

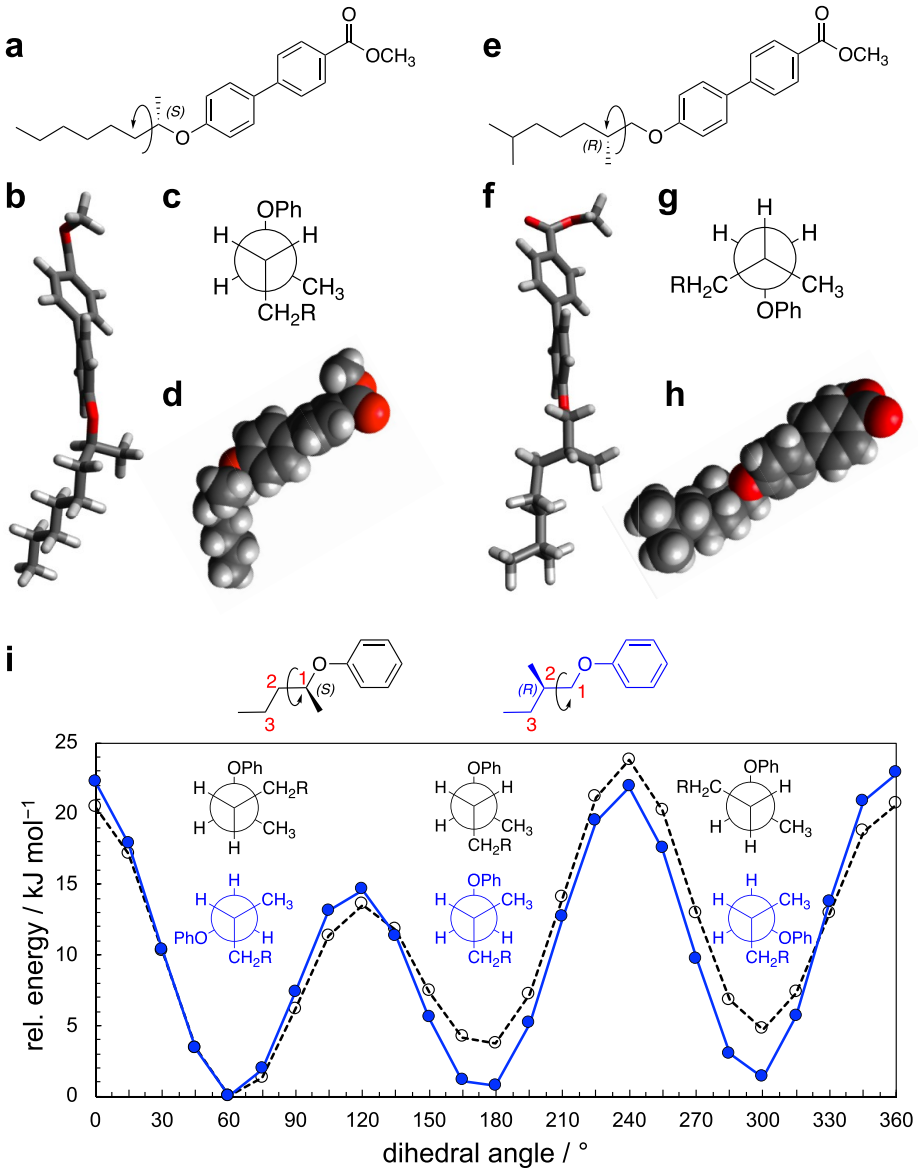

Figure 4. Lowest energy conformations for the molecules representing the arms for the final bent-core compounds with (a−d) (*S*)-2-octyloxy- and (e−h) (*R*)-2,6-dimethylheptyloxy side chain(s). (i) Relative conformational energy profiles for the two substructures with a chiral center at C1 (black open circles and dashed black line) or C2 (blue filled circles and solid blue line) as a function of the dihedral angle defined by O−C1−C2−C3 according to B3LYP/6-31G* calculations.[95,96]

the shorter *meta*- or the longer *para*-side of the molecule, and the resulting molecules are structurally related to compounds **III** and **IV**. Compounds **3**−**5** have (*R*)-2,6-dimethylheptyloxy side chains in each or either the *meta*- or the *para*-side, thereby introducing a chiral center at C2 rather than C1 as well as a terminal branching point at C6. Resembling the branched aliphatic side chain attached to the steroid core of cholesterol, the (*R*)-2,6-dimethylheptyloxy group,[85] as a sulfate isolated from a marine ascidian in the northern Adriatic, is a normonoterpenoid polar metabolite of marine organisms.[86] Despite the additional branching point at C6, the introduction of this chiral moiety does not alter the length of the chiral aliphatic chains in comparison to the structurally related compounds **II**−**IV** with (*S*)-2-octyloxy side chains in each or either the *meta*- or the *para*-side, respectively, and the chiral center (or centers in the case of compounds **II** and **3**) is consistently positioned *de facto* on the same side of the molecule. The expectation is that the indicated structural changes in the chiral side chains will affect the overall molecular conformation and, as a result thereof, potentially the morphology of the B4 building blocks. However, a confluence of altered molecular conformation and diminished chirality could also directly result in the formation of B4 nano- or microfilaments with gradually decreasing helical pitch, although theoretical models of chirality-frustrated fibers have shown no such correlation. These models rather predicted that increasing lateral dimensions of the resulting fibers lead to progressively larger helical pitch values for these twisted crystalline aggregates.[87−89] The conundrum is what comes first or which characteristic controls the other.

RESULTS AND DISCUSSION

Before proceeding to describe and discuss the synthesis and characterization of these materials, we performed some basic

https://doi.org/10.1021/acsnano.1c00527
ACS Nano 2021, 15, 7249−7270

Scheme 1. Comparison of Phase Sequence, Phase Structure, Formed B4 Morphology, and Phase Transition Temperatures Depending on the Chemical Structure (i.e., Length of Aliphatic Side Chains, Position, and Number of Chiral Center(s)), of Compounds 1−5 with the Parent Compounds I−IV[a]

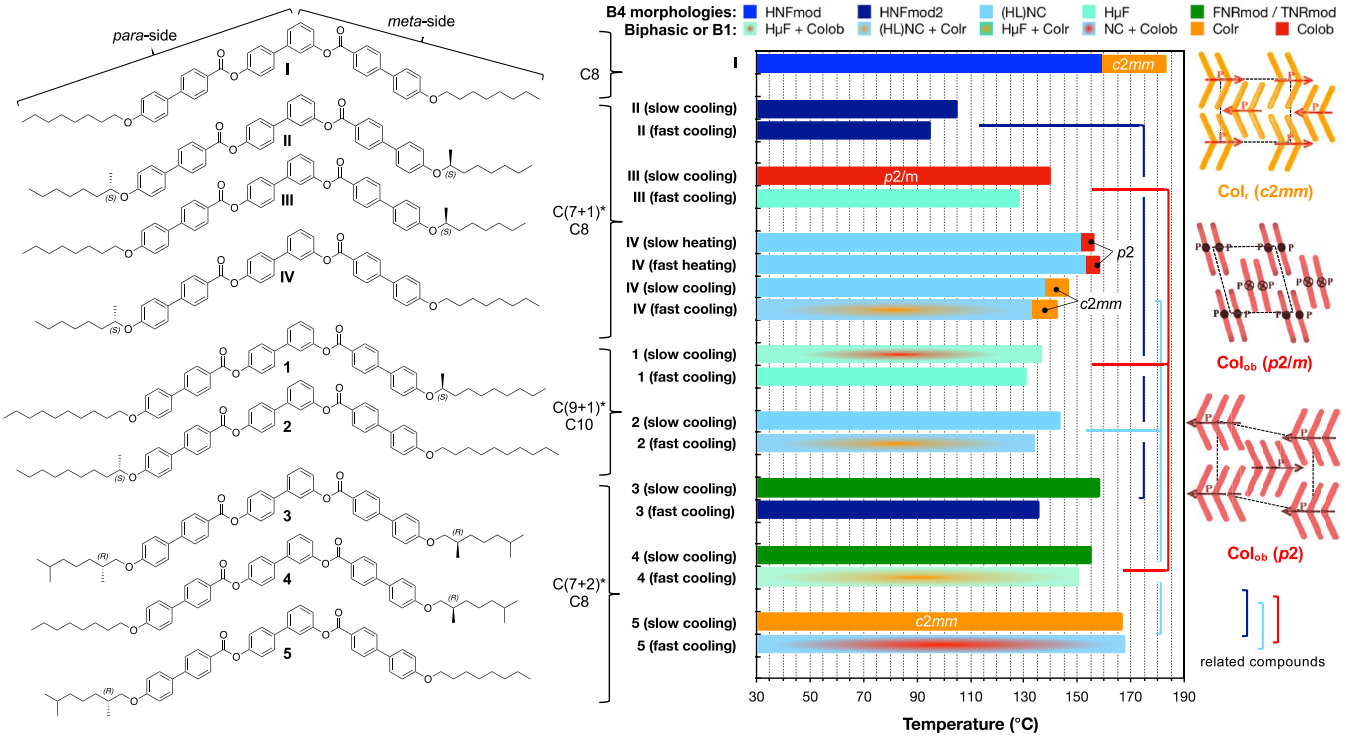

[a]Models for the different B1 phase structures with *c2mm*, *p2/m*, and *p2* are shown at right. Related compounds are identified by the use of colored brackets, and the color coding in the bar diagram is used throughout for the various B4 morphologies and B1 and B4 phases as well as in the CD spectral plots.

computational analyses (using the MMFF94, Merck Molecular Force Field)[90−94] and then calculated the conformational energy profiles of the dihedral angle distribution about the C1−C2 bond axis (at the B3LYP/6-31G* level)[95,96] for simplified side arms containing chiral centers at either C1 or C2, respectively, representative for the (*S*)-2-octyloxy and the (*R*)-2,6-dimethylheptyloxy side chains.

Already the basic computational conformational analysis data have direct consequences for the overall shape of the molecules. The angle θ at the core-chain juncture, recognized as critical for the formation of finite twisted layers with zero Gaussian curvature (local saddle splay)[54] or heliconical layers with cylindrical (zero Gaussian) curvature,[79] is markedly different for the molecules representing the arms of the bent-core molecules with either one of these chiral side chains. The chiral center at C1 for the (*S*)-2-octyloxy side chain promotes a noticeably smaller core-chain angle with a noticeable bend at the core-chain juncture (Figure 4a−d) than the chiral center at C2 for the (*R*)-2,6-dimethylheptyloxy side chain, which results in an almost linear overall shape (Figure 4e−h). In addition, the branching at C6 of the latter also appears to bury the chiral center at the midpoint of this substructure as seen in Figure 4h. Calculations of the relative conformational energy profiles as a function of the dihedral angle, previously used successfully to ascertain the role of conformation in smectic layer structures[97] and here defined by O−C1−C2−C3 (according to B3LYP/6-31G*; Figure 4i), shows clear differences in the relative energies of the possible conformers (dihedral angles with energetic minima). When the chiral center is located at C1, the conformer with a dihedral angle of 60° shows a local energy minimum. However, with the aliphatic chain of the full bent-core molecule being longer, the energetically next lowest conformer with a dihedral angle of 90° should be relevant as well. As predicted,[83] when the chiral center is located at C2, all reasonable dihedral angles of 60°, 180°, and 300° are energetically equal, providing a path to the more rod-like overall conformation, as shown in Figure 4h, thereby supporting the above-described experimental observations that led to the assumption of a diminishing role of chirality when the chiral center is moved farther away from the core to C2.[83] As a result, these conformational analyses foreshadow significant consequences for the morphology of the anticipated B4 phases as well as for the phase sequences overall. Diminishing the role and effects of the chiral centers could potentially lead to morphologies not reported heretofore such as flat ribbons or ribbons with a larger helical pitch, lead to the formation of conglomerates despite molecular chirality, alter the internal structure of the phase, or affect the previously observed polymorphism[76] that considerably depended on the rate of cooling from the isotropic liquid phase.

The synthesis and all analytical data for compounds **1−5** are provided in the Supporting Information (SI, Section S1, Scheme S1 and Figures S1−S10). All purified target compounds **1−5** were then investigated by polarized optical microscopy (POM), differential scanning calorimetry (DSC), and scanning and transmission electron microscopy (SEM and TEM) as well as thin-film circular dichroism (CD) spectropolarimetry and X-ray diffraction (XRD) with synchrotron sources. To study the expected polymorphism, phase coexistence, and variations in morphology depending on the

https://doi.org/10.1021/acsnano.1c00527
ACS Nano 2021, 15, 7249−7270

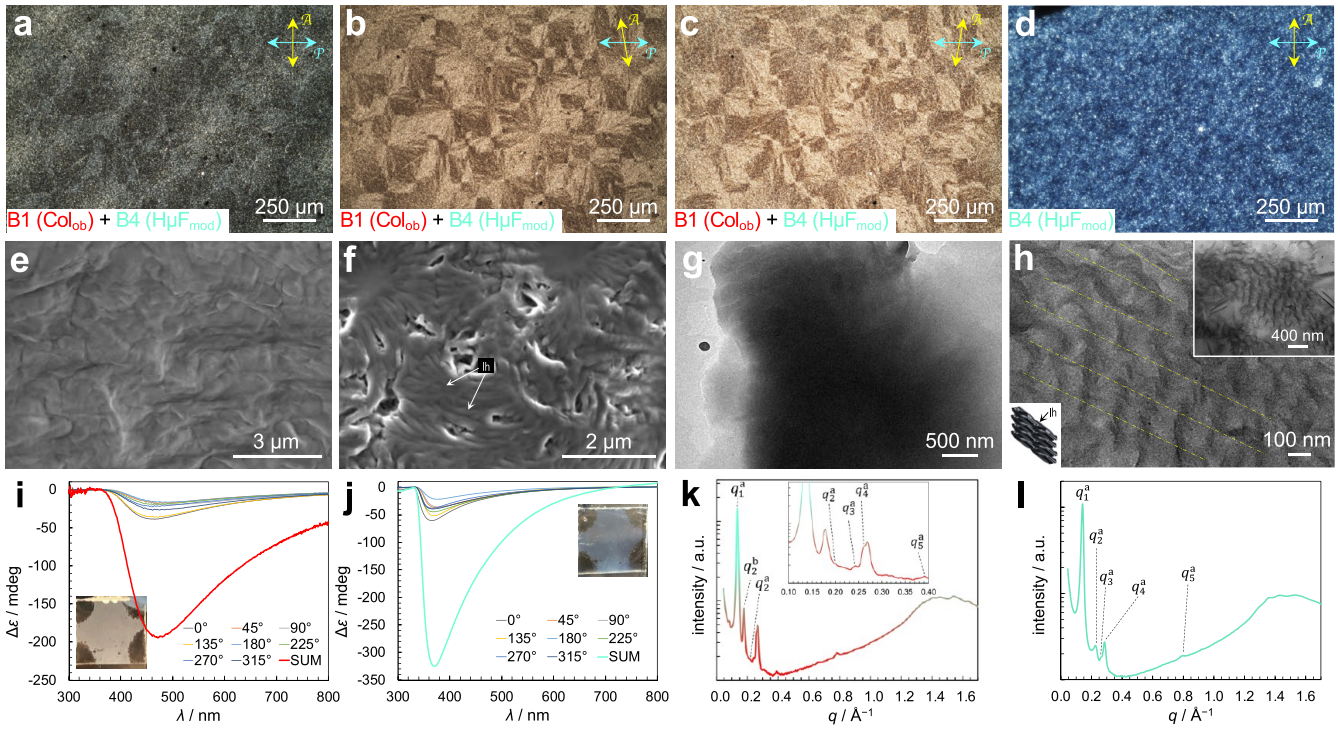

Figure 5. Compound 1: Polarized optical photomicrographs after heating to the isotropic liquid phase (>140 °C) and subsequent cooling to room temperature (~20 °C) upon: (a) slow cooling; crossed polarizers, (b, c) slow cooling; ±5° decrossed polarizers, and (d) fast cooling; crossed polarizers. SEM images after heating to the isotropic liquid phase followed by cooling to room temperature upon: (e) slow cooling and (f) rapid cooling. TEM images obtained after: (g) slow cooling and (h) fast cooling; dashed yellow lines indicate visible separation between parallel and partially overlapping left-handed microfilaments, also highlighted in the model; inset shows section with lower magnification (see also SI, Section S2, Figure S13a,b). Thin-film CD spectra (Δε [mdeg] *vs* λ [nm]) of 10 μm films between untreated quartz substrates after cooling at different cooling rates from the isotropic liquid phase to room temperature at different sample rotation angles, as indicated in the legends (the red and teal curve are the sum-CD spectra to cancel out linear dichroism and birefringence):[100] (i) slow cooling; inset shows sample image lacking blue structural color (white sample is seen) and (j) rapid cooling; inset shows sample image displaying blue structural color. XRD analysis data showing intensity (au) *vs* wave vector *q* (Å^{-1}): (k) slow cooling (inset shows the small-angle region and additional peak assignments) and (l) fast cooling. Peak positions, Miller indices, and relative intensity values are summarized in the SI, Section S2, Figure S14. For color coding in plots, see Scheme 1.

cooling rate, previously observed for the parent materials **I**–**IV**, each of these imaging, thermal, spectroscopic and structural analysis techniques was executed for compounds **1**–**5** both upon slow (5 °C min^{-1}) and upon rapid cooling (≥50 °C min^{-1}) from the isotropic liquid phase. Finally, self-assembly of compounds **3**–**5** was also studied in colloidal dispersion formed in *n*-hexane based on earlier observations of filament formation in dispersions (gels) matching those formed of the neat compounds formed upon cooling from the isotropic liquid state of the B4 phase forming bent-core compounds.[77,79,98]

Scheme 1 provides a preliminary, comparative overview of the data (phase sequence and phase transition temperatures as well as phase and morphology assignment) obtained by POM, DSC, XRD, and electron microscopy for the two sets of compounds: the parent set of **I**–**IV** (Figure 1) and the current set of **1**–**5** (Figure 3). In what follows, we individually discuss each compound and compare the data with those that are structurally closely related.

Side Chain Elongation. Compound **1** is structurally related to **III**[76] and features a chiral center in the shorter *meta*-side of the molecule with an (*S*)-2-decyloxy rather than an (*S*)-2-octyloxy side chain. Upon slow cooling from the isotropic liquid phase, **1** shows a low-birefringence spherulitic-type texture with the typical alternating high- and low-birefringence fans within each spherulitic domain[99] when decrossing the polarizers in opposite directions (Figure 5a–c), typically observed for B1 columnar phases such as for the Col$_{ob}$–*p*2/*m* phase formed by **III**.[76] Upon rapid cooling, a routinely bluish, grainy texture is observed (Figure 5d), which is similar to the texture formed upon rapid cooling as previously reported for the B4–H*μ*F phase of compound **III**.[76] DSC data obtained for each cooling rate, 5 and 50 °C min^{-1} (SI, Section S2, Figures S11 and S12, and Table S1), further confirmed the formation of only one phase, showing exclusively one exothermic peak in each of these cooling runs. SEM (Figure 5e,f) as well as TEM (Figure 5g,h) continue to support this analogy between **1** and **III** by showing featureless, wavy structures for **1** upon slow cooling and helical filaments upon rapid cooling. As anticipated, given the (*S*)-configuration of the chiral center,[76] the filaments with dimensions of $w \sim 250$ nm (width, height) and a helical pitch, *p*, ranging from 650 to 800 nm are microfilaments with a consistently left-handed twist, best seen in the TEM images shown in Figure 5h and Figure S13 (SI, Section S2). The thin-film CD spectra similarly support the homochirality of the B1 and the B4–H*μ*F phases, with the expected sign of the recorded sum-CD signals considering the configuration of the chiral centers: positive for (*R*)-**III**[76] and negative for (*S*)-**1**. For (*S*)-**1**, however, the maxima of the sum-CD signals shifted to lower wavelengths (by about 50–60 nm in each case; λ_{max} = 470 nm in Figure 4i

https://doi.org/10.1021/acsnano.1c00527
ACS Nano 2021, 15, 7249–7270

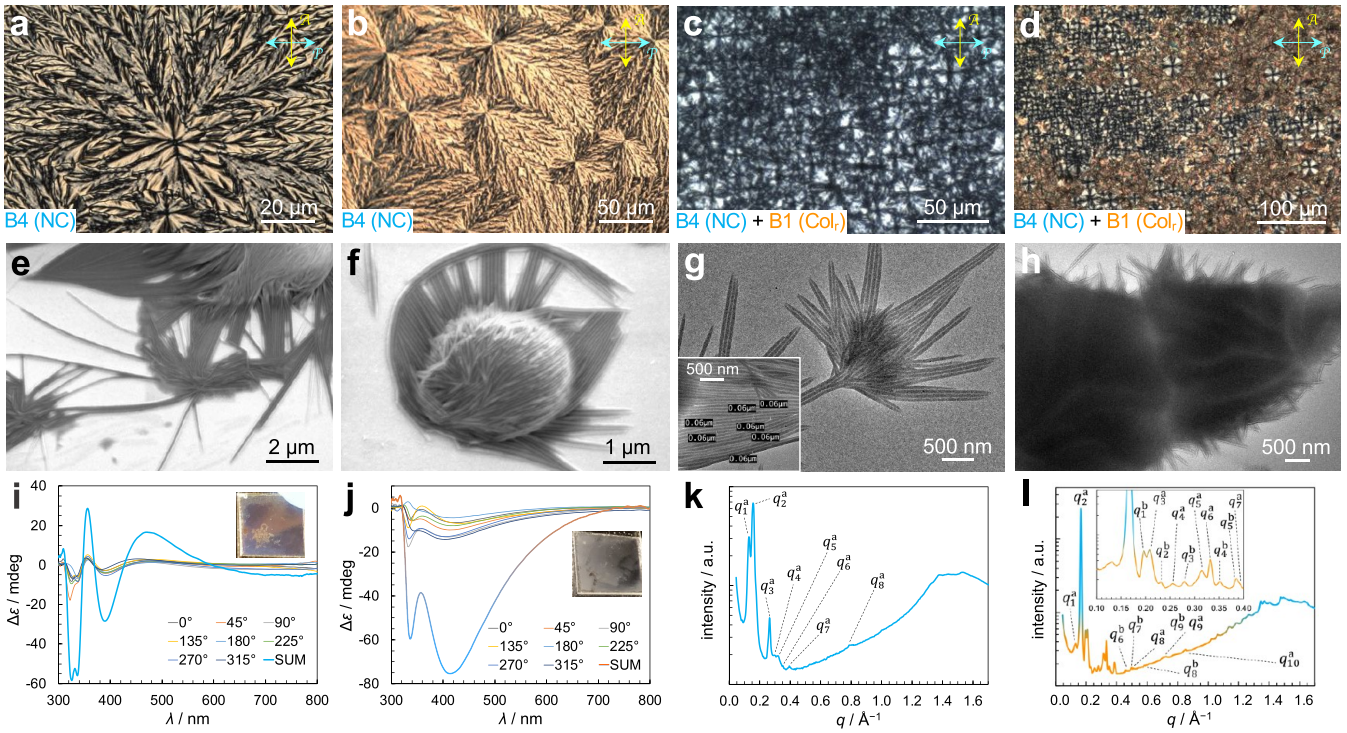

Figure 6. Compound 2: Polarized optical photomicrographs (crossed polarizers) after heating to the isotropic liquid phase (>150 °C) and subsequent cooling to room temperature (~20 °C) upon: (a) slow cooling at higher magnification, (b) slow cooling at lower magnification, (c) fast cooling at higher magnification, and (d) fast cooling at lower magnification showing some indication of biphasic behavior (two interlaced textures). SEM images after heating to the isotropic liquid phase followed by cooling to room temperature upon: (e, f) slow cooling. TEM images obtained after: (g) slow cooling; inset shows another area on the TEM grid showing the constant width (diameter) of the nanocylinders (~60 nm) measured using ImageJ[103] and (h) fast cooling showing features of nanocylinders and wavy solid sections supporting the biphasic behavior seen in (d) by POM. Thin-film CD spectra ($\Delta\varepsilon$ [mdeg] *vs* λ [nm]) of 10 μm films between untreated quartz substrates after cooling at different rates from the isotropic liquid phase to room temperature at different sample rotation angles as indicated in the legends (the light blue and gradient orange-light blue curve are the sum-CD spectra to cancel out linear dichroism and birefringence): (i) slow cooling; inset shows sample image with faint blue structural color and (j) rapid cooling; inset shows sample image with even more faint blue structural color likely due to phase coexistence. XRD analysis data showing intensity (au) *vs* wave vector q (Å^{-1}): (k) slow cooling and (l) fast cooling (inset shows the small-angle region and additional peak assignments). Peak positions, Miller indices, and relative intensity values are summarized in the SI, Section S3, Figure S23. For color coding in plots, see Scheme 1.

and λ_{max} = 370 nm in Figure 5j) in comparison to the sum-CD signals recorded for (*R*)-**III**, for each the Col$_{ob}$–$p2/m$ and the HμF phase.[76] The cause of this hypsochromic shift observed for (*S*)-**1** could be a different orientation of the domains since these CD signals are likely caused by a combination of molecular chirality, in-layer chirality (undulated layers in the case of the Col$_{ob}$ phase and twisted layers in the case of the HμF phase), and packing of the filaments in the case of the HμF phase. The latter contribution found support from the peak position at about λ_{max} = 420 nm that matched the structural color seen by naked eye and measured by UV–vis spectroscopy in reflection mode.[76]

To characterize the structures formed by compound **1** upon rapid or slow cooling, we performed synchrotron XRD experiments (see Methods section for details). Summaries of the obtained XRD data are shown in Figure 5k,l. On slow cooling from the isotropic liquid phase, (*S*)-**1** shows diffraction peaks labeled q_1^a–q_5^a with $q_3^a = \sqrt{q_1^{a2} + q_2^{a2}}$, whereby q_2^a is of lower intensity in comparison to q_1^a and q_3^a, $q_4^a = 2q_1^a$, and $q_5^a = 4q_1^a$, indicating a modulated layer structure (layer spacing d = 46.5 Å) similar to data reported earlier for the B4–HμF phase formed by compound **III** upon rapid cooling (Figure 5k).[76] The precise phase formed by compound **1** is therefore a B4–HμF$_{mod}$ phase. A comparison to the overall length of the molecule with all-*trans* configuration of the aliphatic chains (l = 51 Å) signifies little tilt within these layers. All additional peaks labeled q_i^b (i = 1–8) can be indexed as (001), (100), (10$\bar{1}$), (101), (010), (002), ($\bar{2}$01), and (201) with oblique lattice parameters of a = 34.3 Å, b = 20.8 Å, c = 38.9 Å, and β = 101° (from ALS data set, see SI Section S2, Figure S14). The symmetry group is monoclinic $p2$ (three-dimensional (3D)), and the phase is an oblique columnar phase (Col$_{ob}$), as shown in Scheme 1 and previously reported for compound **IV** upon slow cooling.[79] This phase therefore coexists with the B4 HμF$_{mod}$ phase and dominates the features in the electron microscopy images as well as the thin-film CD data. Upon rapid cooling, (*S*)-**1** shows five major diffraction peaks labeled q_1^a–q_5^a with peak positions and relative intensities closely matching those recorded for (*S*)-**1** upon slow cooling for the HμF$_{mod}$ phase (Figure 5l). In agreement with the electron microscopy and thin-film CD data, (*S*)-**1** exclusively forms a B4–HμF phase under this fast-cooling regime. Hence, these XRD data show that compound **1**, just like the homologue **III**, forms a B4–HμF phase upon rapid cooling and the B1–Col$_{ob}$ upon slow cooling. Conversely, coexistence between these two phases is now only observed for the slow-cooling regime and not for the fast-cooling regime as reported for compound **III**.[76] Moreover, the space group of the Col$_{ob}$ phase formed upon

https://doi.org/10.1021/acsnano.1c00527
ACS Nano 2021, 15, 7249–7270

slow cooling changed from $p2/m$ to $p2$ (3D) but retained the monoclinic lattice.

Relocating the chiral center in the longer (*S*)-2-decyloxy side chain to the *para*-side of the bent-core molecule furnishes compound **2**, which we will initially compare to the parent compound **IV**[79] with a shorter (*S*)-2-octyloxy side chain. On slow cooling from the isotropic liquid phase to room temperature (at a rate of 5 °C min^{-1}), the optical texture of **1** with a feather-like spherulitic appearance (Figure 6a,b shows two different magnifications) closely resembles the textures obtained for compound **IV** upon slow cooling,[79] thereby providing initial evidence of the formation of a B4 HLNC morphology. On rapid cooling (at a rate of ∼50 °C min^{-1}), consistent with the observations reported earlier for **IV**, compound **2** appears to show coexistence of two optical textures, one with lower (Figure 6c) and one with higher birefringence (Figure 6d with lower magnification shows the two coexisting textures with the less birefringent texture characterized by the spherulitic domains seen upon slow cooling). Thorough characterization of the phase structure and morphology of compound **IV** upon rapid cooling revealed that the B4 HLNC coexists with the B1 (Col_r–$c2mm$) phase in this cooling regime,[79] and POM studies of compound **2** appear to support a similar phase behavior. Strikingly different and independent of the cooling rate, POM and DSC data for **2** (SI, Section S3, Figures S15 and S16 and Table S2) show only one phase transition on cooling from the isotropic liquid phase and no formation of a high temperature B1 phase (*i.e.*, also no polymorphism between the Col_{ob} on heating and Col_r on cooling) previously reported for **IV** (Scheme 1).[79]

Such disappearance of the high-temperature B1 phase is supported by data obtained for analogue tris-biphenyl derivatives with nonbranched aliphatic side chains.[73] The derivative with C7 aliphatic chains only forms the B1 and no B4 phase, and the temperature range of the B1 phase (ΔT_{B1}) on cooling is reduced from ∼24 to 9 °C to 3 °C as the chain elongates from C8 to C9 to C10, respectively. Branching just one of the aliphatic chains in **2** prevents the formation of the B1 phase just like the branched aliphatic chains on either side of compound **II**[77] hindered the formation of the B1 phase when compared to the nonbranched parent derivative, compound **I** (Scheme 1). Elongation of the aliphatic chains for the nonbranched derivatives (such as compound **I**) also facilitated lower phase transition temperatures from the isotropic liquid to the B1 liquid crystal phase, $T_{Iso\text{-}B1}$, from 183 °C for C8 and 175 °C for C9 to 167 °C for C10.[73] The same is observed here for **2** featuring longer aliphatic chains. The phase transition temperature of the transition from the isotropic liquid presumably to the B4 phase ($T_{Iso\text{-}B4}$) when compared to **IV** with shorter side chains is reduced.

SEM (Figure 6e,f) and TEM (Figure 6g,h) imaging support phase and morphology assignment for compound **2**, clearly showing nanocylinders displaying the rich hierarchical self-assembly behavior especially for the slow cooling regime already reported for compound **IV**.[79] Numerous of these hierarchical assemblies resemble the blossoms of thistles, pasque flowers or dandelions (Figure 6g and Figure S17 and S18); others resemble three-dimensional objects like coconuts (Figure 6f). Despite a noticeable similarity in appearance of these nanocylinders formed by **2** and **IV**, there are also significant differences. For one, the nanocylinders formed by **2** are consistently smaller in diameter (60 nm for **2**, see insert in Figure 6g, *vs* 80 nm for **IV**[79]). In several of the TEM images, such 60 nm nanocylinders with an average length of 10 or more microns are observed (Figure S19). Given the increased overall length of the bent core molecules with longer aliphatic chains on either side of **2** (l = 5.1 nm), these nanocylinders now consist of only ∼6 concentrical layers rather than 10 layers that made up the HLCNs formed by **IV**. Second, and especially noteworthy, the current nanocylinders formed by **2** upon slow cooling almost entirely lack the clearly discernible heliconical layering (SI, Section S3, Figure S20) observed for the nanocylinders (or HLNCs) formed by **IV**.[79] At the very least, these features are not visible in the TEM images, and only very sporadically in the SEM images for rapidly cooled **2** when no metal is deposited for the SEM sample preparation (SI, Section S3, Figure S21). When visible, however, the right-handedness seen is in line with the (*S*)-configuration of the chiral center in the *para*-aliphatic side chain. Considering this lack of consistent heliconical layering observed for **2**, one could interpret this as a visual indication that elongation of aliphatic chains with a chiral center at the core-chain juncture diminishes the effects of the chiral center and that this results in the largely observed lack of heliconical layering or a significant increase in the helical pitch p. Related cylinder or tubular superstructures with no evidence of heliconical layering were reported by others previously for achiral bent-core compounds in colloidal dispersions (gels) using organic solvents[98,101] or in the case of ionic bent-core materials after self-assembly in water.[102]

Upon rapid cooling of **2** from the isotropic liquid, SEM (SI, Section S3, Figure S22) and TEM (Figure 6h) images show a combination of featureless, smooth regions that are decorated with cylinder-like shapes, thereby indicating what was already reported for compound **IV**[79] and the same cooling regime, phase coexistence.

The thin-film CD data also support these arguments in light of the data reported earlier for compound (*R*)-**IV**. Upon slow cooling, the obtained sum-CD spectrum for (*S*)-**2** (Figure 6i) is basically a mirror image spectrum of the one obtained for (*R*)-**IV**,[79] which is anticipated considering the opposite configuration of the involved chiral centers. The CD bands for (*S*)-**2** are less intense than the ones observed for (*R*)-**IV**, and the intensity distribution of the four either positive or negative bands differs as well. With the CD bands likely arising from a combination of intra- and interlayer chirality as well as any conceivable assembly of the resulting chiral building blocks, it is currently unclear if the lack of heliconical wrapping is causing these minor differences in the two CD spectra of (*S*)-**2** and (*R*)-**IV**. The sum-CD spectrum obtained on rapid cooling (Figure 6j) supports the phase coexistence and with the B1 columnar phase, considering the narrow band centered around λ_{max} = 330 nm (with negative sign, just like the same band observed upon slow cooling) indicative of the B4 nanocylinders and the broad negative band with a maximum centered around λ_{max} = 420 nm, indicating the B1 phase (just like the B1 phase of (*S*)-**1**, and of opposite sign when compared to the sum-CD spectra obtained for (*R*)-**IV**).[79] Curiously, while the B1 phase is not formed as a separate phase at a temperature above the B4 phase, it appears to be the dominant phase judging from the thin-film CD data, as was evident in the SEM and TEM images upon rapid cooling.

Final confirmation of the phase structures was sought by XRD. On slow cooling from the isotropic liquid phase, (*S*)-**2** shows diffraction peaks labeled q_1^a–q_8^a with $q_3^a = 2q_1^a$, $q_5^a = 2q_2^a$, $q_7^a = 3q_1^a$, and $q_8^a = 6q_1^a$ (Figure 6k) indicating a modulated B4

https://doi.org/10.1021/acsnano.1c00527
ACS Nano 2021, 15, 7249–7270

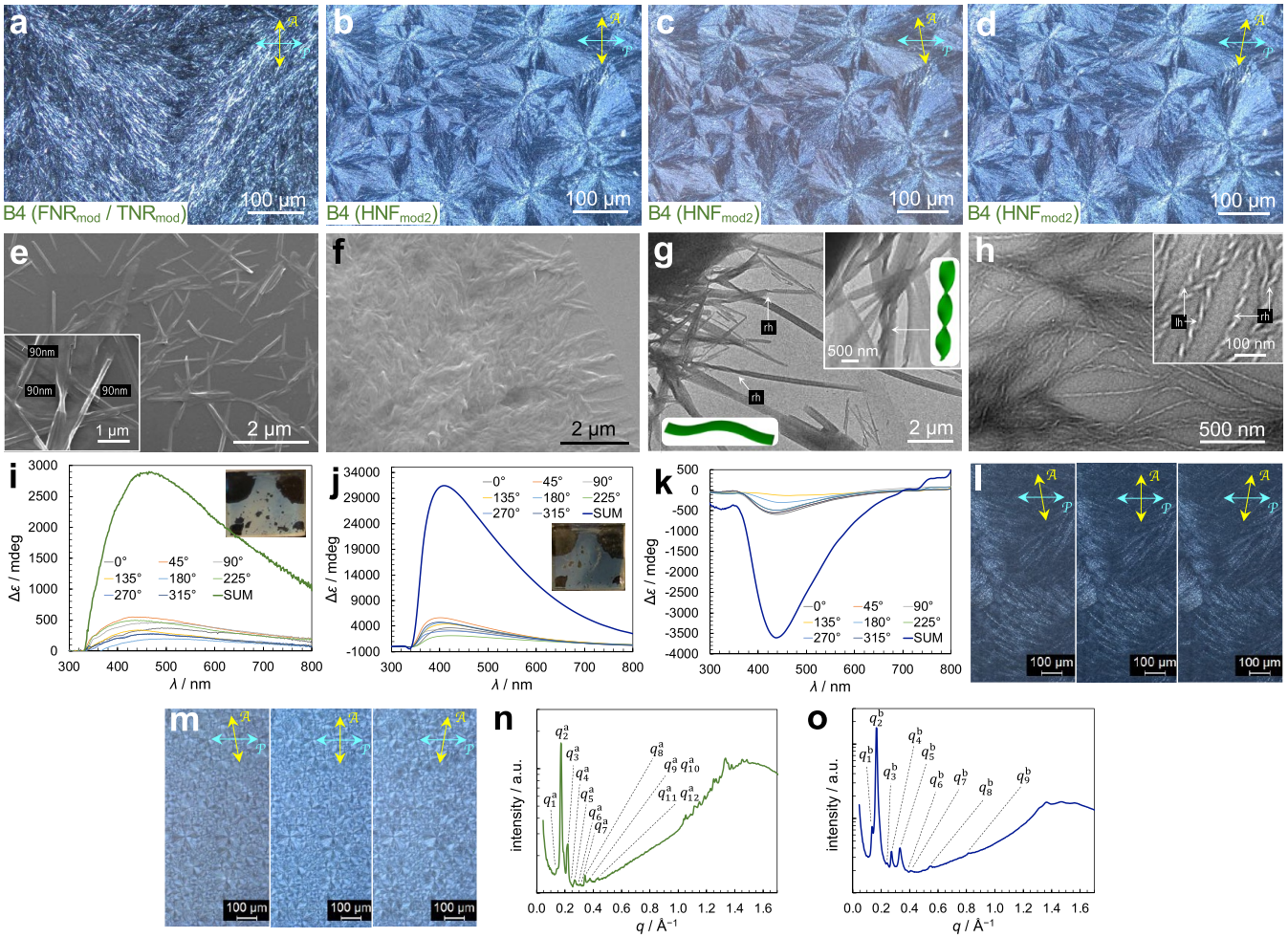

Figure 7. Compound 3: Polarized optical photomicrographs after heating to the isotropic liquid phase (>165 °C) and subsequent cooling to room temperature (~20 °C) upon: (a) slow cooling, (b) fast cooling, (c, d) fast cooling; ±5° decrossed polarizers. SEM images after heating to the isotropic liquid phase followed by cooling to room temperature upon: (e) slow cooling and (f) rapid cooling; inset shows SEM at higher magnification with width measurement data. TEM images obtained after: (g) slow cooling; inserts show a model of a FNR and an image of another area on the TEM grid with TNRs and FNRs as well as a model of the TNRs; height was measured at twisting locations (~40 nm) using ImageJ[103] and (h) fast cooling showing right-handed (rh) and left-handed (lh) HNFs; inset shows a magnified section. Thin-film CD spectra (Δε [mdeg] *vs* λ [nm]) of 10 μm films between untreated quartz substrates after cooling at different cooling rates from the isotropic liquid phase to room temperature at different sample rotation angles as indicated in the legends (the green and dark blue curves are the sum-CD spectra to cancel out linear dichroism and birefringence): (i) slow cooling; inset shows sample image with blue structural color, (j) rapid cooling of one homochiral domain; inset shows sample image with blue structural color, and (k) another homochiral domain with opposite handedness. Zoomed out POM images (magnification: 4×) of the 10 μm CD samples between quartz slides showing the lack of clearly discernible homochiral domains with opposite handedness, as visualized by decrossing polarizer and analyzer upon: (l) slow cooling and (m) fast cooling. XRD analysis data showing intensity (au) *vs* wave vector *q* (Å^{-1}): (n) slow cooling and (o) fast cooling. Peak positions, relative intensity values, and Miller indices are summarized in the SI, Section S4, Figure S28. For color coding in plots, see Scheme 1.

layered nanocylinder structure with a layer spacing of d = 48.0 Å closely matching the calculated molecular length of **2** (l = 51 Å; assuming all-*trans* configurations of the aliphatic chains). The noncommensurate high-q peaks indicate a crystalline structure within these layers typical for B4 phases. This diffraction pattern differs from the homologue with shorter aliphatic chains reported previously (compound **IV**), which displayed no such inlayer modulation.[79]

Upon rapid cooling (Figure 6l), all diffraction peaks labeled q_1^a–q_8^a reappear, clearly indicating the presence of the B4 phase nanocylinders seen by TEM. Here, $q_3^a = \sqrt{q_1^{a2} + q_2^{a2}}$, and $q_4^a = 2q_1^a$, $q_6^a = 2q_2^a$, and $q_7^a = 3q_1^a$ again indicate an intralayer modulated layer structure. An additional set q_1^b–q_9^b, however, indicates coexistence with another phase, which was already seen by POM, thin-film CD, and in the electron microscopy images. These peaks are best indexed as (101), (002), (200), (202), (103), (203), (302), (304), and (006) of a rectangular lattice with *c2mm* plane group (two-dimensional (2D)) and lattice parameters of a = 44.9 Å and c = 53.8 Å. The q_i^b diffraction pattern subset would be in close agreement with the phase coexistence and phase assignment made previously for the lower homologue upon rapid cooling, compound **IV**, with shorter aliphatic chains and therefore applicably smaller lattice parameters of the coexisting Col$_r$–*c2mm* phase (a = 44.7 Å and c = 40.9 Å).[79]

Overall, the phase behavior and identified morphologies of the B4 filaments displayed by compounds **1** and **2** largely

https://doi.org/10.1021/acsnano.1c00527
ACS Nano 2021, 15, 7249–7270

resemble those reported earlier for compounds **III** and **IV**, including the unique polymorphism depending on the cooling rate for compounds **III** and **1**. The configuration of the chiral center in **1**, despite the elongated side chain, continues to determine the handedness of the formed HμFs, a morphology that is essentially controlled by the larger bend angle θ of the core-chain junction in the molecules' *meta*-side that contains the chiral center. In contrast, elongation of the chiral side chain has the most significant consequences for the properties of compound **2**. Here, nanocylinders, exclusively formed upon slow cooling, no longer show any significant indication of heliconical layering. If longer aliphatic tails effectively diminish the effects of chirality and one additionally considers that lower bend angles at the core-chain juncture reduce the tendency to twist,[54,79] this observation is perhaps not surprising. This also leads directly to the next set of compounds (**3**–**5**) with the chiral center relocated from C1 to C2 and an additional branching point in the aliphatic side chain at C6, which imparts even larger bend angles at the core-chain juncture.

Relocation of the Chiral Center and Further Branching. Compound **3** with two (*R*)-2,6-dimethylheptyloxy side chains is structurally most closely related to compound **II**, and this pair should provide initial insights into the consequences of chiral center relocation for these B4 phase forming compounds. Upon slow cooling, POM images show a distinct blue feather-like texture (Figure 7a). After rapid cooling to room temperature, blue spherulitic domains with a local nematic texture[104] are observed, characterized by an alternating birefringence of the fans within each spherulitic domain when decrossing the polarizers in either direction (Figure 7b–d). This likely indicates a radial orientation of the anticipated nanofilaments within these domains.[104] DSC data support the formation of just one phase on cooling from the isotropic liquid phase at rates of 5 as well as 50 °C min^{-1} that persists to room temperature without crystallization. As for all other compounds, rapid cooling led to a lower phase transition temperature and broader peaks in the DSC runs (SI, Section S4, Figure S24 and Table S3).

With the bluish color observed by POM potentially signaling the existence of B4 morphologies, SEM and TEM imaging confirmed this hypothesis. For the slow cooled sample of **3**, SEM surprisingly showed what appeared to be flat ribbon-like shapes (Figure 7e) with a recurrent width of w = 90 nm (although several with larger width are clearly visible as well; insert Figure 7e and Figure S25a,b in the SI, Section S4) and a frequent length of several microns. Upon rapid cooling, the appearance and dimensions of the observed filaments match those commonly reported for HNFs ($w \sim 40$ nm and $p \sim 200$ nm). However, both left- and right-handed HNFs are seen, which is noteworthy in light of the homochiral nature of compound **3** (Figure 7f as well as Figure S25c,d in the SI, Section S4).

TEM images then provide more clarity of what these shapes look like. Upon slow cooling, TEM images of **3** confirm the flat ribbon-like nature of the filaments (ranging in width from w = 90 nm to w = 300 nm); most are flat and straight and some several tens of microns long (image and model in Figure 7g). Others, however, are twisted or helical ribbons that are usually right-handed with a pitch $p \sim 2$ μm (Figure 7g and inset showing several twisted ribbons and a model; see also SI, Section S4, Figure S26). Turning or twisting locations of some of these ribbons also allowed measurements (by image analysis) of the height of these flat ribbons of ∼40 nm, matching the width and height of HNFs. Considering the molecular length of compound **3**, $l \sim 4.5$ nm, the nanoribbons are composed of ∼9 layers. These flat or twisted nanoribbons (we will refer to them as FNRs and TNRs) are among the last and until now missing morphologies for the B4 phase. This is perhaps surprising when considering that such morphologies are known among all possible chiral self-assembly modes of layer structures into helical, heliconical, and twisted morphologies formed by a wealth of structurally unrelated materials including Gemini[55] and other surfactants,[105] a large variety of amphiphilic or polyphilic molecules,[12] bile acid end-modified oligo(*p*-phenylene ethynylene),[106] or naphthalene diimide[107] derivatives among others, and inorganic[108] as well as carbon-based nanomaterials.[109−111] The self-assembly of Gemini surfactants—two identical cationic surfactants connected by an aliphatic hydrocarbon spacer—with chiral counteranions as described by Oda *et al.* serve as prime examples for the consequences of diminished effects of chirality on the formed self-assembled multilayer ribbons.[55] Successively reducing the enantiomeric excess (ee) of the counteranionic L-tartrate by adding the opposite enantiomer led to an increasing helical pitch of the multilayer twisted ribbons from what resembles a HNF for ee > 99% to an FNR for the racemate. Compound **3** under thermodynamic control (*i.e.*, slow cooling) not only forms FNRs but also some of the intermediate forms with larger pitch since multiple conformers are accessible likely due to the existence of equivalent low-energy conformations with respect to the dihedral angle between C2 and C3 at the core-chain juncture.

TEM analysis of **3** upon rapid cooling corroborates the SEM imaging data, noticeably showing HNFs with the expected dimensions already seen in the SEM images and practically equal occurrence of either a left-handed (lh) or right-handed (rh) twist even among adjacent filaments (Figure 7h and insert; see also SI, Section S4, Figure S27). This is highly unusual given that HNFs commonly grow, chirality persevering,[69] forming clearly distinguishable large homochiral domains with opposite handedness (a conglomerate) when the molecules are achiral and only a single homochiral domain (depending on the configuration of the chiral center(s)) when the molecules are homochiral.[77] For compound **3**, filaments with opposite handedness grow, randomly, right next to one another. Following expected trends based on the (*R*)-configuration of the two chiral centers of compound **3**, the sum-CD signal calculated from the individual linear dichroism spectra shows a positive signal, with a maximum wavelength centered around λ_{max} = 420 nm, that is broad enough to cover most of the visible part of the electromagnetic spectrum (Figure 7i).

The positive sign of this CD band is also in line with expectations for the (*R*)-configurations of the chiral centers of **3**, for example, when compared to the negative band observed for filaments with the most closely related shape, the HμFs formed by (*S*)-**1**[76] (Figure 5j). Given the FNR shape formed upon slow cooling, these CD signals should arise from the intralayer chirality of the system, but in part also from the observed TNRs. As HNFs, these FNRs and TNRs give rise to blue structural color (see insert, Figure 7i). POM images of the thin-film CD sample undergoing slow cooling from the isotropic liquid phase also show no sign of opposite homochiral domains, as indicated by decrossing the polarizers (Figure 7l).

https://doi.org/10.1021/acsnano.1c00527
ACS Nano 2021, 15, 7249−7270

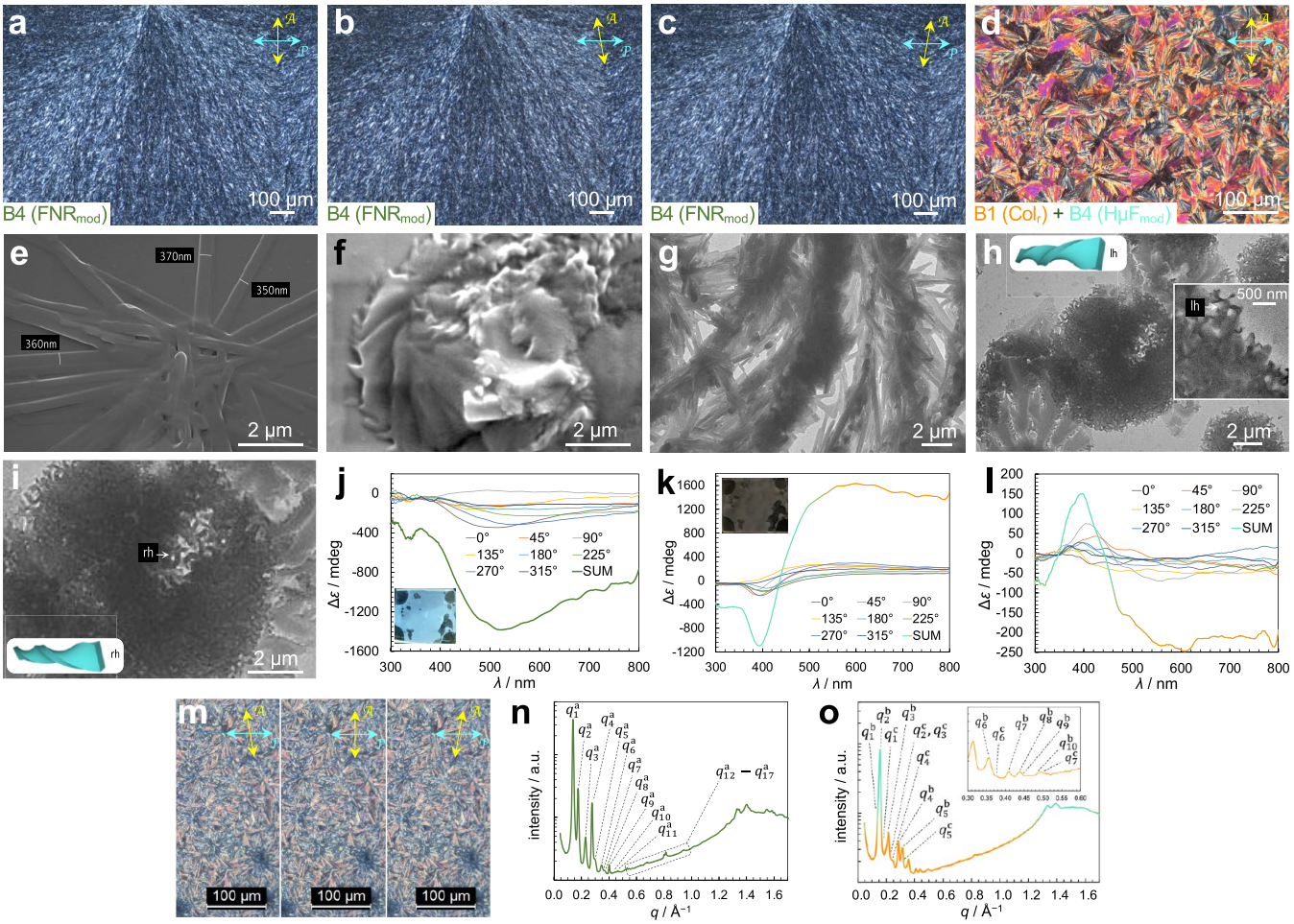

Figure 8. Compound 4: Polarized optical photomicrographs after heating to the isotropic liquid phase (>160 °C) and subsequent cooling to room temperature (~20 °C) upon: (a) slow cooling; crossed polarizers, (b) slow cooling; −8° decrossed polarizers, (c) slow cooling; +8° decrossed polarizers, and (d) fast cooling; crossed polarizers (for images with higher magnification and oppositely decrossed polarizers, see Figure S29, SI). SEM images after heating to the isotropic liquid phase followed by cooling to room temperature upon: (e) slow cooling showing overlapping FNRs; widths averaging $w \sim 360$ nm were measured using ImageJ[103] and (f) rapid cooling showing coexistence of smooth and potentially twisted ribbon-like domains. TEM images obtained after: (g) slow cooling showing overlapping FNRs, (h) fast cooling; inserts show an enlarged section and a potential model of left-handed (lh) twisted ribbons-like structure, and (i) fast cooling and higher magnification showing right-handed (rh) twisted ribbons-like structures; inset show a model. Thin-film CD spectra ($\Delta\varepsilon$ [mdeg] *vs* λ [nm]) of 10 μm films between untreated quartz substrates after cooling at a different rate from the isotropic liquid phase to room temperature at different sample rotation angles as indicated in the legends (the green and red curves are the sum-CD spectra to cancel out linear dichroism and birefringence): (j) slow cooling; inset shows sample image with intense blue structural color, (k) rapid cooling of one sample location; inset shows actual sample lacking structural color, and (l) quasi-mirror imaged spectrum upon rapid cooling of another domain. (m) Zoomed out POM images (magnification: 4×) of the sample between quartz slides interrogated by CD in the rapid cooling regime showing the minor color changes between the low-birefringence domains upon decrossing the polarizers by ±8° (also shown in Figure S30). XRD analysis data showing intensity (au) *vs* wave vector q (Å^{-1}): (n) slow cooling and (o) fast cooling; inset shows the small-angle region and additional peak assignments. Peak positions, relative intensity values, and Miller indices are summarized in the SI, Section S5, Figure S33. For color coding in plots, see Scheme 1.

In contrast, the sum-CD spectra observed for **3** upon rapid cooling show either a positive (Figure 7j) or a negative band (Figure 7k) depending on the particular sample location (spot) interrogated by the ~1 mm diameter light beam. The random growth and spatial coexistence of left- and right-handed HNFs translates into sum-CD signals with opposite signs solely depending on the sample location; by chance positive for sample spots with a significant majority of right-handed HNFs and *vice versa* for sample spots giving a negative sum-CD signal (as proven for compound **II**),[77] thus supporting the colocalization of left- and right-handed HNFs seen by SEM and TEM (Figure 7f and h). The quite variable intensity of the two sum-CD signals shown further supports this argument (Figure 7j and k). Like other HNFs, the HNFs formed by **3** also show blue structural color in reflection mode (see insert, Figure 7j).

POM images of the thin-film CD sample further support this by not showing homochiral domains with opposite handedness by decrossing the polarizers even at the lowest (4×) magnification accessible (Figure 7m). Hence, compound **3** upon rapid cooling appears to form more of a racemic mixture of HNFs (rather than a conglomerate) despite the homochiral nature of the individual molecules.

Because of the shape similarity between HNFs and FNRs or particularly the TNRs, each consisting of ~9 layers (*i.e.*, matching height), as one might anticipate, the maximum

https://doi.org/10.1021/acsnano.1c00527
ACS Nano 2021, 15, 7249−7270

wavelength of the CD band observed for the HNFs (λ_{max} = 410 or 420 nm; Figure 7j,k, respectively) closely matches the maximum wavelengths observed for the FNRs and TNRs with λ_{max} = 420 nm (Figure 7i).

Further analysis of the phase structures was done by XRD. On slow cooling from the isotropic liquid phase (Figure 7n; for q values and relative intensities, see the SI, Section S4, Figure S28a,c), compound **3** shows diffraction peaks labeled q_1^a–q_{12}^a in the small-angle region with $q_5^a = 2q_1^a$, $q_8^a = 2q_2^a$, $q_{11}^a = 3q_1^a$, and $q_3^a = \sqrt{q_1^{a2} + q_2^{a2}}$ (q_4^a and q_6^a are of rather low intensity), indicating a modulated layer structure similar to the B4 HNF_{mod} phase[73] reported earlier. The calculated layer spacing of d = 44.6 Å perfectly matches the calculated molecular length of l = 45 Å signifying that the molecules are positioned orthogonal within the layers, which is likely also a consequence of the larger, almost 180° bend angle θ at the core-chain juncture and the resulting more rod-like shape of both arms of this bent-core molecule. Numerous noncommensurate wide-angle diffraction peaks in the range of q = 1.0–1.6 $Å^{-1}$ suggest a crystalline organization within these layers similar to the other B4 nanofilaments. Thus, aside from the significantly larger dimensions, the XRD data of this phase, now more accurately designated as modulated flat and twisted nanoribbons (FNR_{mod} and TNR_{mod}), indicate that compound **3** with chiral centers in each of the aliphatic side chains forms nanoscale filaments that are structurally and morphologically linked to those formed by their structurally related compounds **I** and **II** (each with identical side chains).

Upon rapid cooling from the isotropic liquid phase, **3** shows diffraction peaks labeled q_1^b–q_9^b with $q_4^b = 2q_1^b$, $q_5^b = 2q_2^b$, and $q_9^b = 6q_1^b$, suggesting a dual-modulated helical nanofilament layer structure (*i.e.*, HNF_{mod2}), akin to the HNF_{mod2} phase reported earlier for compound **II**,[74,77] with a layer spacing d = 46.2 Å (Figure 7o) also closely matching the calculated molecular length (related to the large bend angle at the core-chain juncture causing a more rod-like shape of each molecular side). While less pronounced, noncommensurate wide-angle peaks indicate a crystalline packing within the layers (for q values and relative intensities, see the SI, Section S4, Figures S28b,d,e).

Next, the dual branched (*R*)-2,6-dimethylheptyloxy side chain is present only in the shorter *meta*-side of the molecule, providing compound **4**, which is structurally most closely related to compounds **III** and **1**, each having one chiral center located exclusively in the molecules' *meta*-side and each displaying the recently discovered polymorphism between the B4–HμF and the Col_{ob}–$p2/m$ (B1) phase depending on the cooling rate.[76]

Upon slow cooling, POM images of compound **4** show bluish feather-like texture with local nematic ordering that is likely originating from large spherulitic domains[104] (Figure 8a). Decrossing the polarizers does not locally alter the birefringence in the fan-like domains, that is, the texture remains unchanged when viewed between oppositely decrossed polarizers (Figure 8b,c). Particularly noticeable is the similarity of texture characteristics to those observed for **3** upon slow cooling (Figure 7a). In fact, the two textures practically share many identical features such as the color in transmission considering a comparable sample thickness (*i.e.*, the birefringence), domain sizes, and the overall feather-like appearance. In contrast, the texture observed upon rapid cooling resembles a focal-conic fan texture with significantly elevated birefringence that lacks pseudoisotropic domains (*i.e.*, no dark or black regions with zero birefringence; see Figure 8d). Interlaced with the domains of higher birefringence that do not change in color when decrossing polarizer and analyzer by + 8° or −8°, however, are domains with lower birefringence that do (SI, Section S5, Figures S29 and S30). This could indicate some degree of phase coexistence, which has previously been observed for compounds **III** and **IV**.[76,79] DSC traces again show only one phase transition on cooling at either rate (5 or 50 °C min^{-1}) from the isotropic liquid phase to room temperature with the characteristic lower phase transition temperature as well as a broadening of the peak at the transition from the isotropic liquid phase at the faster cooling rate (SI, Section S5, Figure S31 and Table S4). Thus, the DSC data confirm the observation of only one texture over the entire temperature range as soon as the sample is cooled below the phase transition from the isotropic liquid phase.

SEM images of **4** acquired after slow cooling from the isotropic liquid phase support the textural similarities seen by POM, showing clearly overlapping FNRs with an average width of $w \sim 360$ nm and reaching lengths of several microns (Figure 8e). These are, on average, wider than those observed upon slow cooling for compound **3** but more constant in width (*i.e.*, lower width distribution). Unfortunately, this larger width prevents measurements of the ribbon height and thereby an assessment and comparison of how many layers are stacked, because wider flat ribbons have an increased tendency to lie flat on the substrate. The SEM image obtained after rapid cooling is, however, in stark contrast to the one taken after slow cooling (Figure 8f). Here, flat wavy structures—commonly seen for the columnar phases formed by these bent-core molecules[76,79]—are interlaced with twisted filament-type structures, which seems to support the phase coexistence perceived by POM.

TEM helped to further clarify the situation. TEM images of compound **4** taken after slow cooling show FNRs and further support the observations made by SEM regarding narrow width distribution and average lengths of the FNRs of a few microns. Furthermore, these FNRs bundle up forming stripe-like domains with some degree of splay within each stripe (Figure 8g). The thinner samples of **4** required for and then imaged by TEM after rapid cooling clearly show what was supposed by the SEM and POM imaging data earlier, which is that upon rapid cooling two morphologies (or phases) coexist (Figure 8h). One of these morphologies is characterized by smooth, fern-like shapes (Figure 8h,i), the other by helical filaments with dimensions ($w \sim 250$–300 nm and $p \sim 800$ nm; Figure 8h) matching those of the HμFs reported earlier for compound **III**[76] (Scheme 1) as well as seen here for compound **1** and for each exclusively upon rapid cooling. The major difference between the HμFs formed by compounds **III** and **1** to those formed by compound **4** is that the latter, upon rapid cooling, forms both left- and right-handed HμFs (compare inserts in Figure 8h,i; also see additional TEM images in the SI, Section S5, Figure S32). Similar to the left- and right-handed HNFs formed by compound **3** upon rapid cooling, the HμFs of opposite handedness formed by **4**, despite the (*R*)-configuration of the chiral center in the side chain, give rise to the mirror-imaged thin-film CD bands in different sample locations (Figure 8k,l).

Considering the dense nature and size of the domains visible in the SEM and TEM images, it is currently unclear if these domains are composed of HμFs of just one handedness or if, as for the HNFs formed by **3** upon rapid cooling, HμFs of both

https://doi.org/10.1021/acsnano.1c00527
ACS Nano 2021, 15, 7249–7270

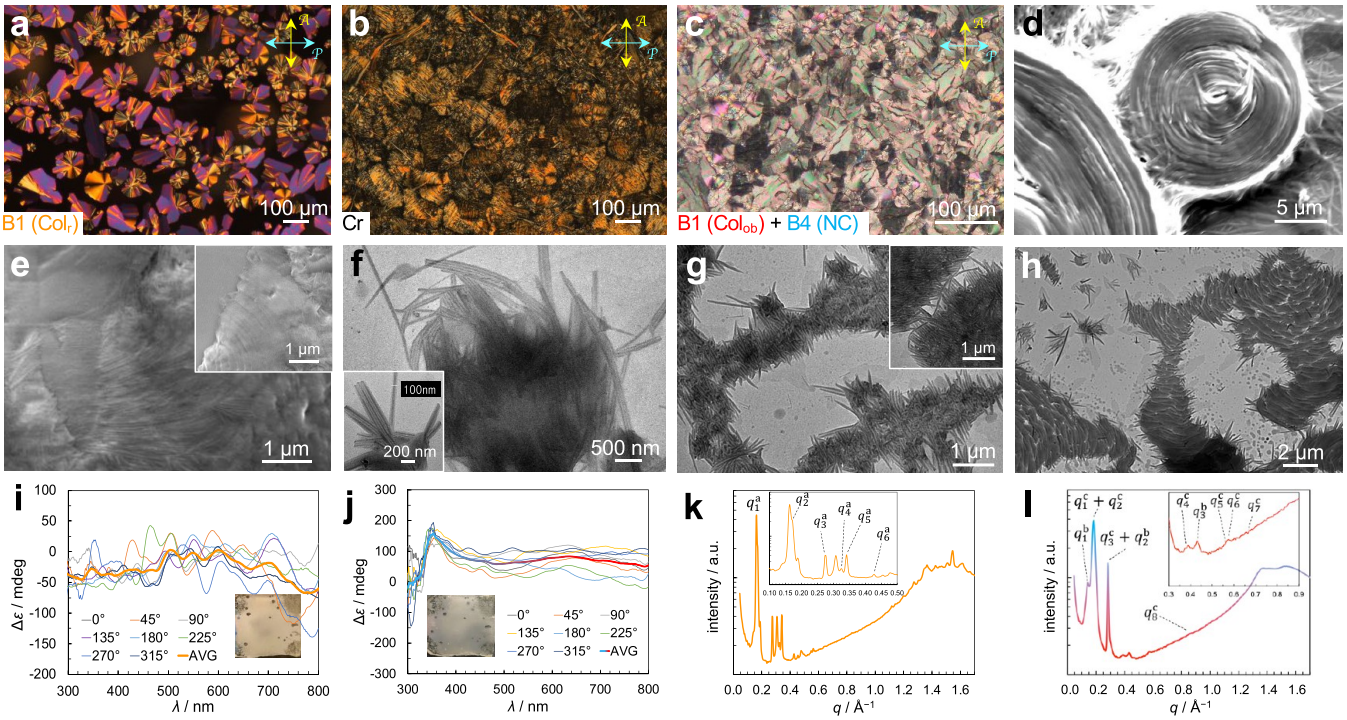

Figure 9. Compound 5: Polarized optical photomicrographs after heating to the isotropic liquid phase (>175 °C): (a) at 168 °C upon slow cooling; crossed polarizers, (b) at further cooling to room temperature (~20 °C); crossed polarizers, (c) at 20 °C upon rapid cooling; crossed polarizers (for photomicrographs at higher magnification indicating color changes upon decrossing the polarizers, see Figure S36, SI). SEM images after heating to the isotropic liquid phase followed by cooling to room temperature upon: (d) slow cooling and (e) rapid cooling showing coexistence of smooth filamentous domains. TEM images obtained after: (f) slow cooling showing what appear to be core−shell fibers; inset show separate section with measurement of one such fiber with a width (or diameter) of ~100 nm as determined by using ImageJ,[103] (g) fast cooling showing a quasi-network of short, needle-like smooth and solid filaments (width of w ~ 60−80 nm); inserts show a slightly enlarged section, and (h) fast cooling showing coexistence of smooth and the same needle-like filaments. Thin-film CD spectra ($\Delta\varepsilon$ [mdeg] *vs* λ [nm]) of 10 μm films between untreated quartz substrates after cooling at a different rate from the isotropic liquid phase to room temperature at different sample rotation angles as indicated in the legends (the orange and red curves are the averaged CD spectra to cancel out linear dichroism and birefringence): (i) slow cooling; inset shows sample image not showing any indication of structural color, (j) rapid cooling with discernible maximum at a wavelength of λ_1 = 350 nm; inset shows a sample photograph with a noticeable blueish hue in reflection. XRD analysis data showing intensity (au) *vs* wave vector q (Å^{-1}): (k) slow cooling and (l) fast cooling; insets show the small angle regions and additional peak assignments. Peak positions, relative intensity values, indexing of the coexisting Col$_{ob}$−$p2$ phase and peak deconvolutions are summarized in the SI, Section S6, Figure S39. For color coding in plots, see Scheme 1.

handedness grow randomly and potentially adjacent to one another within one domain. In either case, a comparison of the area interrogated by CD (beam diameter ~1 mm at the sample) with the domain sizes seen by electron microscopy clearly suggests that there must be a spatially varying concentration of left- and right-handed HμFs giving rise to mirror-image CD spectra with unequal intensities.

Further analysis of the phase structures was done by XRD. On slow cooling from the isotropic liquid phase, compound **4** shows diffraction peaks labeled q_1^a−q_{17}^a (Figure 8n, and SI, Section S5, Figure S33a and S33c) with $q_4^a = 2q_1^a$, $q_6^a = 2q_2^a$, $q_9^a = 3q_1^a$, $q_{12}^a = 3q_2^a$, $q_{17}^a = 6q_1^a$, and a strong diffraction peak $q_3^a = \sqrt{q_1^{a2} + q_2^{a2}}$, suggesting an additional electron density modulation. This diffraction pattern closely matches the one recorded for compound **3** upon slow cooling, with the marked difference being the reversal of the relative intensities of q_1^a and q_2^a, which might be caused by the significant width difference between the FNRs formed by compounds **3** and **4** in the slow-cooling regime. This modulated B4 phase is therefore best abbreviated as FNR$_{mod}$ (two independent electron density waves forming a rectangular lattice),[73] just as the phase formed by compound **3** upon slow cooling, with a layer spacing of d = 45.5 Å that again matches the calculated molecular length (l = 46 Å), thereby indicating an orthogonal orientation of the molecules within the layers.

Upon rapid cooling, the log plot shows two sets of well-resolved peaks, one with ten maxima labeled q_1^b−q_{10}^b with $q_4^b = 2q_1^b$, $q_3^b = \sqrt{q_1^{a2} + q_2^{a2}}$, $q_5^b = 2q_2^b$, and $q_9^b = 3q_1^b$ (Figure 8o and SI, Section S5, Figure S33b,d,f), which closely matches the diffraction patterns recorded for the B4−HμF$_{(mod)}$ phase formed by compounds **1** and **III**,[76] each upon rapid cooling. Furthermore, the layer spacing of d = 42.1 Å for compound **4** closely matches the one reported for **III** (d = 39.05 Å),[76] which one would anticipate given that both compounds are identical with respect to their molecular lengths, and is by the appropriate amount smaller than the layer spacing of the HμF phase formed by compound **1** (d = 44.5 Å). A second set of diffraction peaks labeled q_1^c−q_7^c that are best indexed as (101), (002), (200), (102), (202), (103), and (204) suggest a rectangular lattice with *c2mm* plane group (2D) and lattice parameters of a = 55.5 Å and c = 55.6 Å (practically a square lattice) that are larger than those calculated for the Col$_r$−*c2mm* phases formed by compounds **I**, **IV**, and **2** (perhaps as a result of the more rod-like shape of the *meta*-side of molecule **4**

https://doi.org/10.1021/acsnano.1c00527
ACS Nano 2021, 15, 7249−7270

promoting a slightly altered length to width ratio and thereby a different packing in the rectangular, almost square, lattice). In essence, the XRD data fully support the phase coexistence already seen by POM, thin-film CD, and electron microscopy but, of course, cannot identify the racemic nature of the HμFs seen by TEM imaging. However, among the related compounds **III**, **1**, and **4**, only **4** forms a Col_r phase, while both **III** and **1** form Col_{ob} phases, which could be the consequence of the more rod-like shape of the *meta*-side caused by the chiral center at C2 and the end-branching of the aliphatic side chain at C6.[112]

Finally, the last compound in this second series, compound **5**, sees the dual branched (*R*)-2,6-dimethylheptyloxy side chain in the longer *para*-side of the molecule. Compound **5** is structurally most closely related to compounds **IV** and **2**, each having one chiral center located exclusively in the molecules' *para*-side and each forming the B4 nanocylinder morphology upon slow cooling and a coexistence between the B4-nanocylinder and B1 columnar phase upon rapid cooling.[79] The key differences between these two parent compounds **IV** and **2** with respect to **5** are that only **IV** forms high-temperature B1 phases (with polymorphism between Col_{ob}–*p*2 phase formed on heating and the Col_r–*c2mm* phase on cooling) and that **2** lacks the consistent heliconical layering of the nanocylinders on slow cooling shown previously for **IV**. Contrary to all other compounds described here, **5** shows two phase transitions on each consecutive heating run by DSC (SI, Section S6, Figure S34 and Table S5) as well as by POM at the slow and the rapid cooling rate. On slow heating, the first phase transition (at T = 146 °C), characterized by the larger phase transition enthalpy, is ascribed to a phase transition from the crystalline solid to the liquid crystal phase observed at higher temperatures; the second phase change is to the transition from this liquid crystal to the isotropic liquid phase (clearing point at T_{cl} = 161 °C). The texture of the liquid crystal phase observed by POM on slow heating resembles the texture observed upon subsequent slow cooling (Figure 9a), which crystallizes so quickly (Figure 9b and Figure S35 in the SI) that this second phase transition on slow cooling is not resolved by DSC (only one phase transition peak on cooling with a maximum at T = 168.2 °C, Figure S34, SI). Key features of this texture (Figure 9a) are the low birefringence spherulitic domains and pseudoisotropic regions indicative of a B1 phase[99,113] that disappear once the sample seems to crystallize (or goes through the rapidly occurring second phase transition). For the fast-cooling regime, the DSC traces are, as observed for all other compounds, characterized by broader peaks but occur in the case of compound **5** at near identical phase transition temperatures. The texture observed upon rapid cooling, however, considerably differs from the one seen upon slow cooling.

The few spherulitic domains visible are striated both along and across the spherulites, and no pseudoisotropic regions exist. The texture is best described as a combination of a mosaic texture with higher birefringence (in comparison to the texture seen upon slow cooling) and less birefringent (darker) domains (Figure 9c), whose color intensity at least minimally differs upon decrossing the polarizers in one or the other direction, respectively (SI, Section S6, Figure S36). The latter, darker features suggest a possible phase coexistence between a B1 and a B4 phase as seen already for compound **4** upon rapid cooling (Figure 8d and Figure S29). Generally, all detected textural features imply the formation of columnar (B1-type) phases,[113] lacking many of the characteristic features typically seen for the B4 phase (including all morphologies reported thus far).

SEM imaging, in part, confirms what was construed from POM. Upon slow cooling, spherical domains can be seen with diameters of some of the larger ones measuring tens of microns. These domains appear fuzzy on their periphery and seem to be decorated with cylinder-like filaments with an average width or diameter of w or d = 100–150 nm. The spherical domains themselves more closely resemble vinyl records with concentrical grooves (Figure 9d and Figure S37) and some features more alike to the filaments decorating them.

Upon rapid cooling, SEM imaging confirms the aforementioned coexistence showing both smooth as well as filamentous regions adjacent to one another (Figure 9e). These filaments, with much smaller width or diameter (w or $d \sim$ 80 nm) in comparison to those seen upon slow cooling, now clearly branch as observed previously for the B4 HLNCs formed by **IV**[79] with quite similar diameter. This suggests that compound **5**, like the parent compounds **IV** and **2**, forms nanocylinders upon rapid cooling in coexistence with a B1 phase typically showing smooth features by SEM and TEM imaging. TEM imaging corroborates these findings by showing core–shell-type filaments with a nominal width of $w \sim$ 100 nm growing out of a smooth mass or core (Figure 9f), similar to nanotubular morphologies previously reported for bent-core molecules with acute bend angles when up to 20 wt % of rod-shaped nematic or smectic liquid crystal compounds were admixed.[114] The coaxial (or core–shell) nature is clearly visible by the light-dark-light contrast of each filament (insert, Figure 9f). Upon rapid cooling, TEM images collected for **5** then show regions (resembling arrays) with needle or cylinder-like morphologies ($w \sim$ 80 nm) and regions that are predominantly featureless and smooth, forming arrays (Figure 9h) similar to fish scales that are decorated with the needle- or cylinder-shaped structures (see SI, Section S6, Figure S38 for additional images at higher magnifications). Thus far, compound **5** shows the least resemblance to its parent compounds **IV** and **2** in light of all the microscopy data when compared to compounds **3** and **4**. This trend continues for the thin-film CD data. Upon slow cooling, individual linear dichroism spectra display random maxima and minima close to $\Delta\varepsilon \sim 0$ mdeg (about −20 mdeg to be exact) across the entire wavelength range from 300 to 800 nm (Figure 9i). These individual spectra were therefore averaged, not summed up, to more closely represent what is seen in the individual linear dichroism spectra. Both ways to analyze thin-film CD data of birefringent materials are equivalent (using the average or the sum), but the average seemed in this particular case more informative given the randomness among the spectra taken at the 45° interval sample rotation angles. We conclude that the phase and morphology obtained at slow cooling is CD silent and therefore not of the B4 nature. Further supporting this argument is the fact that the sample shows no blue structural color and appears off-white and semitransparent (insert, Figure 9i). Upon rapid cooling, the thin-film CD data share some of the same features with those seen upon slow cooling but with one major exception: a clearly discernible positive band (maximum in $\Delta\varepsilon$) in the averaged CD signal at a wavelength of λ_1 = 350 nm (Figure 9j). One could even argue that there is another very broad band centered around a wavelength of λ_2 = 640 nm. However, the randomness of the signals in the individual linear dichroism spectra favors the argument that the

https://doi.org/10.1021/acsnano.1c00527
ACS Nano 2021, 15, 7249–7270

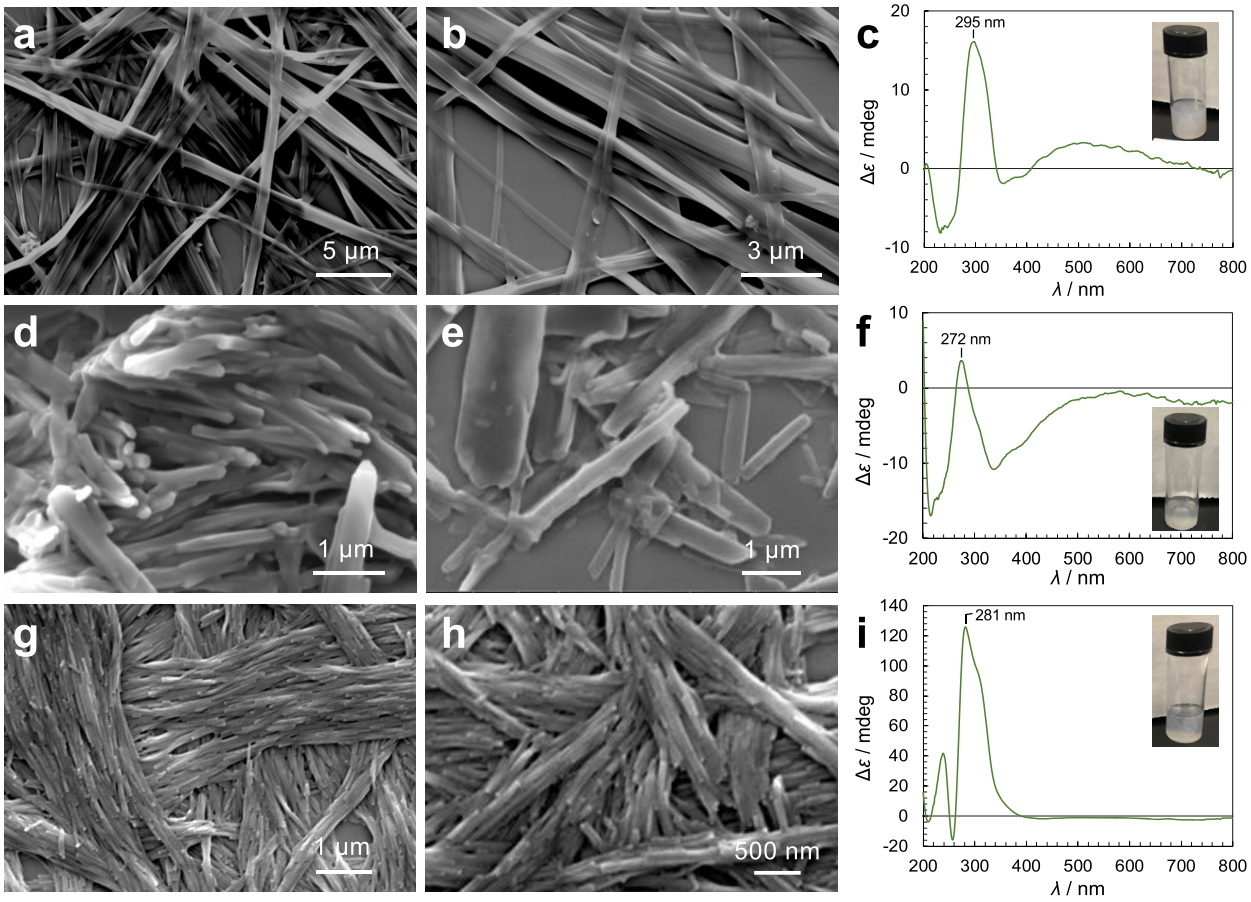

Figure 10. Compounds 3−5 in *n*-hexane: SEM images after drying the *n*-hexane solution on SEM sample holder: (a, b) compound 3, (d, e) compound 4, and (g, h) compound 5. Solution CD spectra of: (c) compound 3, (f) compound 4, and (i) compound 5 in *n*-hexane; each inset shows the formed colloidal dispersion (gels) in a test vial. For color coding in plots, see Scheme 1.

CD signal in the wavelength range from 400 to 800 nm is practically flat, just not averaging, but close to $\Delta\varepsilon = 0$. A comparison to the sum-CD spectra reported for **IV** and seen for **2** reveals the existence of similar bands at $\lambda \sim 350$ nm as well as random maxima at longer wavelength. The sign of the band for compound **5** at this wavelength is positive and therefore opposite to the sign of the potentially related band seen for compound **2** with opposite configuration of the chiral center. However, a relationship between the signs of these two bands seen for compounds **2** and **5**, respectively, is unlikely since the two chiral centers are on different carbon atoms in the aliphatic side chain. If any of the Gray and McDonnell rules were active here, an empirical rule to predict the handedness of a chiral nematic phase depending on the nature, location, and configuration of the chiral center in the aliphatic side chain,[115] one would perhaps expect that the sign of these two bands should be identical, but this is not what is experimentally observed. In essence, the thin-film CD data suggest that compound **5** forms a columnar phase with no chiral signature upon slow cooling and that upon rapid cooling, a B1 columnar and a B4 nanocylinder phase coexist, thus supporting the POM, SEM, and TEM data.

To buttress these arguments, further confirmation of the phase structures was sought by XRD. On slow cooling from the isotropic liquid phase, **5** shows diffraction peaks labeled q_1^a−q_9^a, which can be indexed as (101), (002), (200), (202), (004), (203), (301), (105), and (303) with rectangular lattice parameters of a = 45.5 Å and c = 73.9 Å (q_1^a−q_6^a shown in Figure 9k; all q_i^a (i = 1, ..., 9) in the SI, Section S6, Figure S39a,c). The length of the unit cell a closely matches the one previously reported for compound **IV** (a = 44.7 Å), but the length of the unit cell c is here significantly longer (in comparison to the Col$_r$−$c2mm$ phase formed by **IV**, c = 40.9 Å).[79] The plane group would be $c2mm$ (2D), with the phase designated as a B1 Col$_r$ phase. Possible reasons for this expansion of the unit cell are that the two Col$_r$−$c2mm$ phases of **IV** and **5** were interrogated at markedly different temperatures (room-temperature XRD data used for **5** and ∼150 °C XRD data for **IV**) and that the sample of **5** here has essentially crystallized, only showing remnants of the B1 Col$_r$ phase detected by POM at elevated temperatures, which is also indicated by further, nonassigned peaks in the XRD plot (Figure 9k). Regrettably, compound **5** crystallizes too quickly to permit XRD studies of the Col$_r$ phase upon slow cooling from the isotropic liquid phase (see Figure 9b and Figure S35 in the SI).

Upon fast cooling, and in line with the phase coexistence seen by POM, thin-film CD, and electron microscopy imaging, compound **5** shows two sets of diffraction peaks labeled q_1^b−q_3^b and q_1^c−q_8^c (Figure 9l, and in the SI, Section S6, Figure S39b,d,e). The two intense reflections centered at $\sim q$ = 0.184 Å^{-1} and 0.284 Å^{-1} appear here to be overlapping signals (labeled $q_1^c + q_2^c$ and $q_3^c + q_2^b$), which can be deconvoluted to extract the individual contributions of these electron density

https://doi.org/10.1021/acsnano.1c00527
ACS Nano 2021, 15, 7249−7270

modulations (see SI, Section S6, Figure S39f,g). The diffraction data subset q_i^b (i = 1, ..., 3) with $q_2^b = 2q_1^b$ and $q_3^b = 3q_1^b$ indicates a highly ordered layer structure with a layer spacing of d = 44.0 Å that again matches the calculated molecular length of **5**. This further supports the observation of the nanocylinder morphology of this B4 phase seen by TEM imaging. The remaining diffraction subset q_i^c (i = 1, ..., 8) is best indexed as (001), (100), (101), (200), (202), (010), (111), and (303) with an oblique lattice and monoclinic space group $p2$ (3D). This coexisting $Col_{ob}-p2$ phase, hinted at by POM (Figure 9c) and detected in the form of smooth features by TEM (Figure 9g,h), then features lattice parameters of a = 34.85 Å, b = 11.2 Å, c = 35.2 Å, and β = 103° that are reasonably similar to those calculated for the coexisting Col_{ob} phase formed by compound **1** upon slow cooling (see Figure 5k). Overall, the phase behavior of compound **5** differs significantly from those observed for the related compounds **2** and **IV**, although all the same phases and morphologies are present. On slow cooling, **5** forms exclusively a B1 Col_r-c2mm and no B4 phase morphology at lower temperature like compound **IV** does. Upon rapid cooling, the B4 nanocylinders coexist with a B1 $Col_{ob}-p2$ phase that is solely seen at higher temperature and during the heating cycle for compound **IV** but not at all for compound **2**.

Given this rich polymorphism observed for such a small subset of compounds with bent molecular shape (*i.e.*, the formation of these B4 nano- and microfilaments; stable over months, once isolated), we further examined the self-assembly of some of them in an organic solvent.

Self-Assembly Behavior in Colloidal Dispersions. Previous experimental reports,[98,102,114] including for some of the parent compounds **I**–**IV**,[77,79] show that these types of B4-forming bent-core compounds can form colloidal dispersions (gels) essentially consisting of the same types of building blocks (morphologies) as those formed by the neat compounds when cooled from the melt. Ordinarily, colloid formation and gelation in a suitable organic solvent led to the same, thermodynamically controlled morphologies seen for the neat material upon slow cooling from the melt.[77,79]

Pondering about the quite unusual phase behavior as well as the formation of the FNR and TNR B4-phase morphologies produced by some of the compounds **3**–**5**, we investigated the self-assembly behavior in the as-formed colloidal dispersions (gels) of these three compounds in *n*-hexane. Initially, all three compounds fully dissolve in this organic solvent, but upon standing rapidly transform to a colloidal dispersion. To characterize these colloids, we first performed solution CD experiments and then dried the sample on SEM sample holders (Figure 10).

The SEM images obtained for compound **3** clearly show the FNRs previously seen for this compound upon slow cooling from the isotropic liquid phase with matching widths, ranging from a few hundred nm to about 1 μm. These images convey that these FNRs, after drying, form fiber mats resembling a chaotic network of highways crossing above and underneath one another, and no twist is seen for any of these ribbons (Figure 10a,b).

The solution CD spectrum (a combination of solution CD and CD of the FNR colloids in *n*-hexane) shows two distinct positive CD couplets ($-\Delta\varepsilon \rightarrow +\Delta\varepsilon$) centered at 270 and 410 nm, respectively (Figure 10c). The couplet in the UV region originates from the relative orientational differences between the electric dipole moments of the biphenyl segments[116] imposed by the specific molecular conformation of compound **3** in solution. The couplet in the visible wavelength region is then the result of orientational differences between the arms of these bent-core molecules in the FNRs since it appears at reasonably similar wavelengths (maximum for the positive CD signal at a wavelength of $\lambda \sim$ 490 nm) as the sum-CD maximum found for the thin-films (Figure 7i). Compound **4** then forms rather similar FNR colloids in *n*-hexane, though shorter in average length, seemingly larger in height (judging from those ribbons that orient favorably to see this), and with a larger width distribution (Figure 10d,e). Some of the smallest ribbons visible in these images tend to feature more a round or oval cross-section. Differences in length of the FNRs (or TNRs in the case of compound **3**) have already been observed for compounds **3** and **4** upon slow cooling of the neat materials from the isotropic liquid phase, and thus far, it remains unclear which exact experimental parameters affect the average length of these nanoribbons formed predominantly under thermodynamic control (out of solution or upon slow cooling). The solution CD spectrum of **4** is similar to the one recorded for **3** and differs mainly in relative intensities of the bands (Figure 10f). The positive CD couplet in the UV region is centered at a minimally shorter wavelength of λ = 265 nm; the band in the visible spectral region never crosses zero. Finally, compound **5** forms uniform rod- or cylinder-like objects (Figure 10g,h) that, like for **3**, form dense fiber mats with a local nematic-like ordering. In contrast to compounds **3** and **4** forming FNRs that match those found for the neat compounds upon slow cooling, compound **5** forms this cylinder-like morphology matching one of the morphologies found for neat **5** upon rapid cooling from the melt even with quasi-identical overall dimensions (Figure 9g,h). The solution CD spectrum of **5** also differs from the spectra recorded for **3** and **4**. Now, two apparently negative CD couplets occur, one in the UV-region centered around a wavelength of λ = 250 nm and one in the visible (barely crossing zero) at λ = 385 nm (Figure 10i). Perhaps not surprisingly, adding the solution CD spectra of compounds **4** and **5** (each with one chiral center in the *meta*- or *para*-side of the molecule, respectively), after some normalization of the $\Delta\varepsilon$ maxima, virtually reproduces the solution CD spectrum recorded for compound **3** with a chiral center in each side chain (SI, Section S7, Figure S40). Consequently, while the morphologies formed in these colloidal dispersions differ between **3**, **4**, and **5**, spectropolarimetrically these three materials are indeed additive.

Overall, just like the parent compounds **I**–**IV**, the compounds featuring either one or two (*R*)-2,6-dimethylheptyloxy side chain(s), **3**–**5**, replicate the morphologies earlier found upon slow cooling from the isotropic melt in colloidal dispersions in an organic solvent upon standing. The only exception from the common rule is compound **5**, which forms the morphology in colloidal dispersion otherwise found as part of the morphologies formed upon rapid cooling (*i.e.*, kinetic control) but not on slow cooling.

CONCLUSIONS

In this work, we demonstrate how the interplay between chirality and molecular conformation can be predictably fine-tuned to control the morphology of nanofilaments in B4-phase bent-core compounds. We can conclude that the number of chiral centers and the length of the chiral side chain as well as the position in the molecule overall (longer *para*-, shorter *meta*-side, or both) and in the side chain (C1 or C2 at the

https://doi.org/10.1021/acsnano.1c00527
ACS Nano 2021, 15, 7249–7270

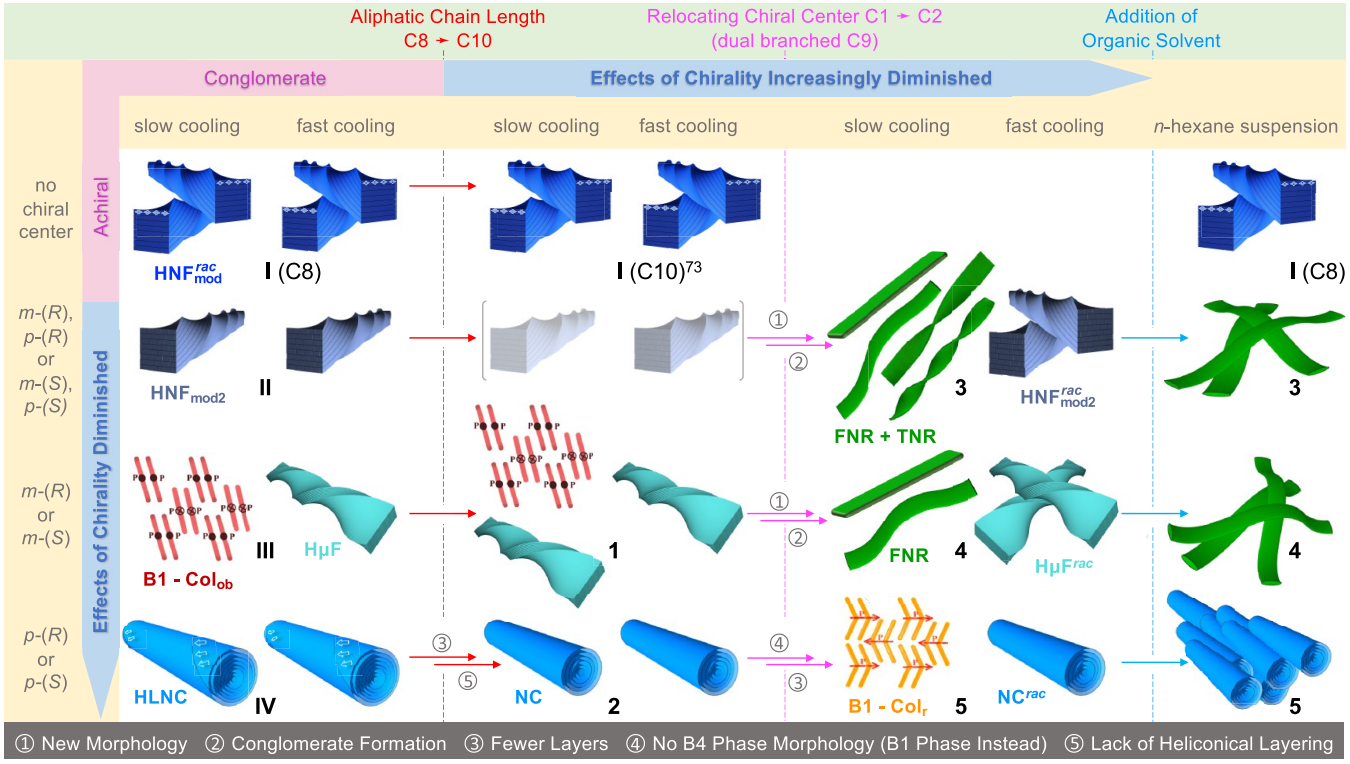

Figure 11. Graphical summary of the phases and B4 morphologies formed by parent compounds I−IV in contrast to compounds 1−5 studied here depending on the structural modifications (*i.e.*, number and position of chiral centers) in the aliphatic side chains and on the ensuing diminished effects of chirality. Other phases than the B4 phase morphology are shown only when no B4 phase is formed; essentially anticipated B4 morphologies, based on the data we have for the homologues series, are shown semitransparent.

core-chain juncture) affect both global and local conformations of the bent-core molecules that, in turn, affect the morphology of the B4 filaments and the phase or phase coexistence seen experimentally. The predicted diminishing effect of chirality, as the chiral center is located away from the core-chain juncture or as the side chain length increases, directly translates to the type of B4 filament formed. HNFs are formed due to an intralayer mismatch between the top and bottom molecular halves of bent-core molecules such as **I** that can only be relieved by local saddle splay with negative Gaussian curvature ($\kappa_1\kappa_2 < 0$). In other words, the global and local conformations of the molecules in these smectic layers spontaneously break the chiral symmetry leading to a twist of the smectic layers. Earlier work by Schnur *et al.*,[117] Ghafouri and Bruinsma,[118] as well as Sharon *et al.*,[119] recently reviewed by Grason,[120] provide detailed and elegant theoretical assessments of the driving forces for these and other geometrically frustrated assemblies. The self-limiting width of HNFs (~40 nm) is discussed in the "high chirality" limit, where a sufficiently large twist elastic constant (K_2) arrests or preselects the helical pitch of the twisted filaments; the self-limiting number of smectic layers is a consequence of the incompatibility between surface curvature and equal layer spacing, that is, equal layer spacing requires that the curvature adjusts as the number of layers increases.[120] Confinement in nanochannels is one option to alter the shape (curvature) of HNFs,[71] adjusting the global and local conformations by strategically positioning chiral centers in these asymmetric bent-core molecules, as shown here. Controlling the effects of the chiral centers on the overall molecular shape by enabling energetically equivalent local conformations at the core-chain juncture provides access to perhaps all the missing B4 nanofilament morphologies, considering the nanofilament shapes (Figure 11) discovered for related systems such as the aforementioned Gemini surfactants[55] or assemblies formed by rod-like fd viruses.[121] In the latter system, just like for the bent-core compounds described here, decreasing the strength of the chiral interactions (by increasing the temperature) permits access to a range of polymorphic forms, from flat 2D membranes for weak chirality to helicoidal twisted membranes in the high chirality regime (low temperature) whose handedness can be controlled by point mutations in the virus.[121]

The crystalline order of the B4 nanofilaments observed by solid-state NMR[122] and frequently by XRD (including for all samples assessed by XRD here) adds further frustration for chiral ordering, as pointed out by Grason,[120] and provides a path from helicoidal (such as in HNFs) to increasingly spiral ribbons (from HμFs to TNRs to HLNCs), where the width is no longer self-limiting as indicated by the commonly larger width of these B4 morphologies. When the effects of chirality are greatly diminished, ribbons that are only sporadically twisted and flat nanoribbons emerge. Overall, relocating the chiral center and simultaneously adding another branching point are more conducive for the B4 filament shape to deviate from the classical HNF morphology, that is, moving away from the high chirality regime, than increasing the length of the chiral aliphatic chain (Figure 11).

Finally, thermal annealing (or slow cooling) and rapid thermal quenching (fast cooling) provide another level of control over the phase and morphology formed. For the molecules with elongated chains (**1** and **2**), the most drastic consequence is the lack of heliconical layering observed for **2**

https://doi.org/10.1021/acsnano.1c00527
ACS Nano 2021, 15, 7249−7270

with respect to the parent molecule **IV**. For the dual-branched compounds **3**–**5**, rapid cooling produces either the racemate of the morphology observed by the parent molecules (*i.e.*, a conglomerate with presumably equal portions of right- and left-handed filaments) or filaments lacking heliconical layering, here dubbed racemic nanocylinders (*rac*) (Figure 11). Slow cooling leads to the formation of ribbons, either flat, twisted, wavy, or even undulated, as is the case of the formation of the Col_r–*c2mm* phase by **5** upon slow cooling.

The conformational freedom in the dual-branched chiral side chain(s) in **3** and **4**, particularly upon slow cooling, that is, in the thermodynamic regime, is clearly revealed in the random degree of twist of the nanoribbons from perfectly flat FNRs over occasionally to periodically twisted TNRs (Figure 12).

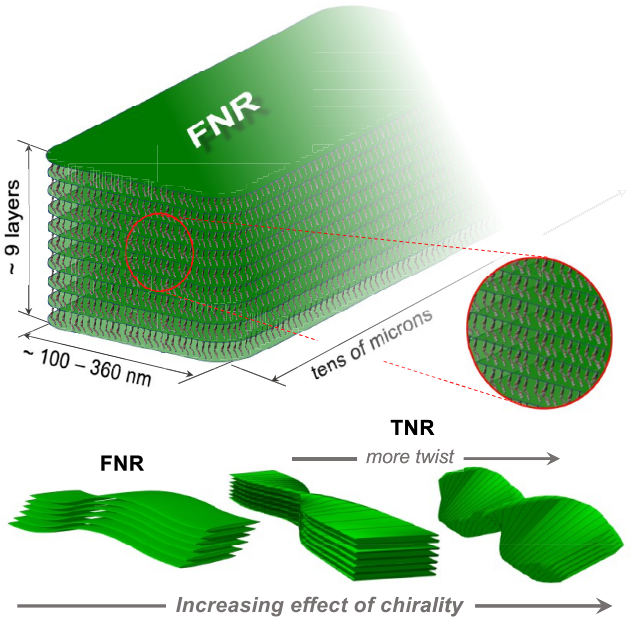

Figure 12. Models of flat and twisted nanoribbons (FNRs and TNRs) formed by compounds 3 and 4 upon slow cooling and in dispersions with *n*-hexane. TNRs are formed exclusively by 3 (higher chirality regime) and are absent for 4 (lower chirality regime) on slow cooling from the isotropic melt. In colloidal dispersions with *n*-hexane, likely due to swelling of aliphatic sublayers, both 3 and 4 form exclusively FNRs.

Thermal annealing usually leads to the formation of thermodynamically more stable polymorphs, thereby favoring the formation of the wider nanoribbons expected for the lower chirality regime. These morphologies are then essentially reproduced in colloidal dispersions formed upon standing in an organic solvent. Finally, the wealth of twisted structures and morphologies with predictive control over the helical pitch and other overall dimensions will provide a suitable and versatile platform for the chiral assembly of a range of materials, from nanoparticles[123] to emissive dyes[80] and quantum dots,[124] that can further be controlled by the addition of chiral additives.[75]

METHODS

Optical and Thermal Characterization. Polarized optical microscopy (POM) observations were carried out under an Olympus BX-53 polarizing microscope equipped with a Linkam LTS420E heating/cooling stage. Samples were heated above the clearing point as indicated by differential scanning calorimeter (DSC) and then cooled at either <5 °C min^{-1} (commonly 2 °C min^{-1}; slow cooling) or ~50 °C min^{-1}. Phase transition temperatures and enthalpies were determined using a PerkinElmer Pyris 1 DSC at two heating and cooling rates (5 °C min^{-1} and 50 °C min^{-1}), reporting data from the second heating and cooling runs, respectively. Temperatures are calibrated with indium and zinc as standards.

Spectroscopy. Thin-film circular dichroism (CD) spectropolarimetry was performed using an OLIS spectrophotometer with quartz substrates. To eliminate contributions from linear dichroism and birefringence, all samples and sample areas were investigated at 45° interval sample rotation angles. The spectra were then summed up or averaged to provide genuine CD signals of the sample area. The area interrogated by the light beam, given by the instrumental slit size and shape, is ~0.4 cm in diameter and larger than most individual domains seen by POM of the samples sandwiched between two quartz substrates using nominal spacers of 10 μm.

X-ray Diffraction. Variable-angle X-ray diffraction was carried out at the SMI beamline of the National Synchrotron Light Source II (NSLS-II) at the Brookhaven National Laboratory (BNL) with a beam energy of 16 keV (beam: 400 mA, spot size of 2.2 × 25 μm, 1 mm capillaries in vacuum) and on beamline 7.3.3 of the Advanced Light Source (ALS) of Lawrence Berkeley National Laboratory[125] (10 keV incident beam energy, 1.24 Å wavelength, utilizing a Pilatus 2 M detector). At the ALS (beam: 500 mA, 10 s exposure, spot size of 250 × 800 μm, in air and between Kapton windows), materials were filled into 1 mm diameter quartz X-ray capillary tubes, which were then mounted into a custom-built aluminum cassette that allowed X-ray detection with ±13.5° angular range. A silver behenate standard was used to calibrate the detector distance and beam center, and the calibrated 2D images were converted to radially integrated 1D curves using the NIKA SAXS data reduction software.[126] At BNL, scattering patterns were collected on an in-vacuum Pilatus 1 M detector, consisting of 0.172 mm square pixels in a 941 × 1043 array, and the exposure time was set to one second. Data were acquired at both BNL and ALS because of the difference in spot size with respect to the relative dimensions of the domains in samples showing phase coexistence (more local *vs* more global data sets).

Scanning and Transmission Electron Microscopy. SEM analysis was performed using a Quanta 450 FEG SEM with or without prior metal deposition as noted. TEM was carried out on an FEI Tecnai F20 microscope, operating at 200 kV and equipped with a Schottky field emission gun and a twin-blade anticontaminator. All images were recorded using a Gatan 4K Ultra Scan charge-coupled device camera. Since these organic material films are sensitive to the electron beam irradiation, the films were normally previewed rapidly at a dose of 20 e^- nm^{-2}. Selected areas were then imaged at a dose level of 200 e^- nm^{-2}, which did not cause radiation damage. A drop of a solution of each compound in an organic solvent such as ethylene chloride (or *n*-hexane for the colloidal dispersions) was placed on either indium tin oxide substrates for SEM or grids for TEM. After complete evaporation of the solvent in vacuum, the sample was heated and cooled as described for the POM experiments.

ASSOCIATED CONTENT

Supporting Information

The Supporting Information is available free of charge at https://pubs.acs.org/doi/10.1021/acsnano.1c00527.

Details of the syntheses and all analytical data (^1H and ^{13}C NMR, elemental analysis) of compounds **1**–**5**; additional POM, SEM, and TEM images as well as CD and XRD data (PDF)

AUTHOR INFORMATION

Corresponding Author

Torsten Hegmann – *Materials Science Graduate Program, Kent State University, Kent, Ohio 44242-0001, United States; Advanced Materials and Liquid Crystal Institute, Department of Biological Sciences, Brain Health Research*

https://doi.org/10.1021/acsnano.1c00527
ACS Nano 2021, 15, 7249–7270

Institute, and Department of Chemistry and Biochemistry, Kent State University, Kent, Ohio 44242-0001, United States; orcid.org/0000-0002-6664-6598; Email: thegmann@kent.edu

Authors

Jiao Liu – *Materials Science Graduate Program, Kent State University, Kent, Ohio 44242-0001, United States; Advanced Materials and Liquid Crystal Institute, Kent State University, Kent, Ohio 44242-0001, United States*

Sasan Shadpour – *Materials Science Graduate Program, Kent State University, Kent, Ohio 44242-0001, United States; Advanced Materials and Liquid Crystal Institute, Kent State University, Kent, Ohio 44242-0001, United States*

Marianne E. Prévôt – *Advanced Materials and Liquid Crystal Institute, Kent State University, Kent, Ohio 44242-0001, United States*

Michael Chirgwin – *Advanced Materials and Liquid Crystal Institute, Kent State University, Kent, Ohio 44242-0001, United States*

Ahlam Nemati – *Materials Science Graduate Program, Kent State University, Kent, Ohio 44242-0001, United States; Advanced Materials and Liquid Crystal Institute, Kent State University, Kent, Ohio 44242-0001, United States;* orcid.org/0000-0003-0282-2027

Elda Hegmann – *Materials Science Graduate Program, Kent State University, Kent, Ohio 44242-0001, United States; Advanced Materials and Liquid Crystal Institute, Department of Biological Sciences, and Brain Health Research Institute, Kent State University, Kent, Ohio 44242-0001, United States;* orcid.org/0000-0003-3287-5103

Robert P. Lemieux – *Department of Chemistry, University of Waterloo, Waterloo,, Ontario N2L 3G1, Canada*

Complete contact information is available at: https://pubs.acs.org/10.1021/acsnano.1c00527

Author Contributions

T.H. and J.L. conceived the described experiments. J.L. and M.C. with the help of S.S. and A.N. performed the syntheses and analytical characterization of the materials. J.L., M.C., and S.S. performed the POM and SEM studies, A.N. performed all the TEM experiments, and J.L. and A.N. performed the CD experiments. M.E.P. and E.H. performed the XRD studies. M.E.P., E.H., and T.H. analyzed the XRD data. R.P.L. calculated the conformational energy profiles. T.H. directed the research and wrote the manuscript with contributions from all coauthors.

Notes

The authors declare no competing financial interest.

ACKNOWLEDGMENTS

This work was supported by the U.S. National Science Foundation (NSF; DMR-1506018, CHE-1659571, and DMR-1904091), the Ohio Third Frontier (OTF) program for Ohio Research Scholars "Research Cluster on Surfaces in Advanced Materials" (T.H.), which also supports the Materials Characterization and Imaging facility at the Advanced Materials and Liquid Crystal Institute at Kent State University, where current SEM and TEM data were acquired. R.P.L. acknowledges funding from the Natural Sciences and Engineering Research Council of Canada (NSERC). The authors are also grateful for access to the SAXS beamline at the Advanced Light Source, which is supported by the Director (Office of Science, Office of Basic Energy Sciences) of the U.S. Department of Energy under contract no. DE-AC02-05CH11231. Finally, this research used resources of the National Synchrotron Light Source II, a U.S. Department of Energy (DOE) Office of Science User Facility operated for the DOE Office of Science by Brookhaven National Laboratory under contract no. DE-SC0012704.

REFERENCES

(1) Cao, Z. L.; Gao, H.; Qiu, M.; Jin, W.; Deng, S. Z.; Wong, K. Y.; Lei, D. Y. Chirality Transfer from Sub-Nanometer Biochemical Molecules to Sub-Micrometer Plasmonic Metastructures: Physiochemical Mechanisms, Biosensing, and Bioimaging Opportunities. *Adv. Mater.* **2020**, *32* (41), 1907151.

(2) Jahani, S.; Jacob, Z. All-Dielectric Metamaterials. *Nat. Nanotechnol.* **2016**, *11* (1), 23–36.

(3) Xing, P. Y.; Zhao, Y. L. Controlling Supramolecular Chirality in Multicomponent Self-Assembled Systems. *Acc. Chem. Res.* **2018**, *51* (9), 2324–2334.

(4) Liu, M. H.; Zhang, L.; Wang, T. Y. Supramolecular Chirality in Self-Assembled Systems. *Chem. Rev.* **2015**, *115* (15), 7304–7397.

(5) Mateos-Timoneda, M. A.; Crego-Calama, M.; Reinhoudt, D. N. Supramolecular Chirality of Self-Assembled Systems in Solution. *Chem. Soc. Rev.* **2004**, *33* (6), 363–372.

(6) Chen, Y.; Ma, W. T. The Origin of Biological Homochirality along with the Origin of Life. *PLoS Comput. Biol.* **2020**, *16* (1), No. e1007592.

(7) Suzuki, N.; Itabashi, Y. Possible Roles of Amphiphilic Molecules in the Origin of Biological Homochirality. *Symmetry* **2019**, *11* (8), 966.

(8) Tamura, K. Perspectives on the Origin of Biological Homochirality on Earth. *J. Mol. Evol.* **2019**, *87* (4–6), 143–146.

(9) Blackmond, D. G. The Origin of Biological Homochirality. *Cold Spring Harbor Perspect. Biol.* **2019**, *11* (3), a032540.

(10) Blackmond, D. G. The Origin of Biological Homochirality. *Philos. Trans. R. Soc., B* **2011**, *366* (1580), 2878–2884.

(11) Blackmond, D. G. The Origin of Biological Homochirality. *Cold Spring Harbor Perspect. Biol.* **2010**, *2* (5), a002147.

(12) Yashima, E.; Ousaka, N.; Taura, D.; Shimomura, K.; Ikai, T.; Maeda, K. Supramolecular Helical Systems: Helical Assemblies of Small Molecules, Foldamers, and Polymers with Chiral Amplification and Their Functions. *Chem. Rev.* **2016**, *116* (22), 13752–13990.

(13) Xiao, L.; An, T. T.; Wang, L.; Xu, X. L.; Sun, H. D. Novel Properties and Applications of Chiral Inorganic Nanostructures. *Nano Today* **2020**, *30*, 100824.

(14) Ma, W.; Xu, L. G.; de Moura, A. F.; Wu, X. L.; Kuang, H.; Xu, C. L.; Kotov, N. A. Chiral Inorganic Nanostructures. *Chem. Rev.* **2017**, *117* (12), 8041–8093.

(15) Ben-Moshe, A.; Wolf, S. G.; Bar Sadan, M.; Houben, L.; Fan, Z. Y.; Govorov, A. O.; Markovich, G. Enantioselective Control of Lattice and Shape Chirality in Inorganic Nanostructures using Chiral Biomolecules. *Nat. Commun.* **2014**, *5*, 4302.

(16) Liu, Y.; Wang, J.; Kim, S.; Sun, H. Y.; Yang, F. Y.; Fang, Z. X.; Tamura, N.; Zhang, R. P.; Song, X. H.; Wen, J. G.; Xu, B. Z.; Wang, M.; Lin, S. R.; Yu, Q.; Tom, K. B.; Deng, Y.; Turner, J.; Chan, E.; Jin, D. F.; Ritchie, R. O.; et al. Helical van der Waals Crystals with Discretized Eshelby Twist. *Nature* **2019**, *570* (7761), 358–362.

(17) Nemati, A.; Shadpour, S.; Querciagrossa, L.; Li, L.; Mori, T.; Gao, M.; Zannoni, C.; Hegmann, T. Chirality Amplification by Desymmetrization of Chiral Ligand-Capped Nanoparticles to Nanorods Quantified in Soft Condensed Matter. *Nat. Commun.* **2018**, *9*, 3908.

(18) Jana, M. K.; Song, R.; Liu, H.; Khanal, D. R.; Janke, S. M.; Zhao, R.; Liu, C.; Valy Vardeny, Z.; Blum, V.; Mitzi, D. B. Organic-to-Inorganic Structural Chirality Transfer in a 2D Hybrid Perovskite and Impact on Rashba-Dresselhaus Spin-Orbit Coupling. *Nat. Commun.* **2020**, *11* (1), 4699.

(19) Peng, Y.; Yao, Y. P.; Li, L. N.; Liu, X. T.; Zhang, X. Y.; Wu, Z. Y.; Wang, S. S.; Ji, C. M.; Zhang, W. C.; Luo, J. H. Exploration of Chiral Organic-Inorganic Hybrid Semiconducting Lead Halides. *Chem. - Asian J.* **2019**, *14* (13), 2273−2277.
(20) Huc, I. Aromatic Oligoamide Foldamers. *Eur. J. Org. Chem.* **2004**, *2004* (1), 17−29.
(21) Hirschberg, J. H. K. K.; Brunsveld, L.; Ramzi, A.; Vekemans, J. A. J. M.; Sijbesma, R. P.; Meijer, E. W. Helical Self-Assembled Polymers from Cooperative Stacking of Hydrogen-Bonded Pairs. *Nature* **2000**, *407* (6801), 167−170.
(22) Zhou, Y. L.; Marson, R. L.; van Anders, G.; Zhu, J.; Ma, G. X.; Ercius, P.; Sun, K.; Yeom, B.; Glotzer, S. C.; Kotov, N. A. Biomimetic Hierarchical Assembly of Helical Supraparticles from Chiral Nanoparticles. *ACS Nano* **2016**, *10* (3), 3248−3256.
(23) Guerrero-Martinez, A.; Auguie, B.; Alonso-Gomez, J. L.; Dzolic, Z.; Gomez-Grana, S.; Zinic, M.; Cid, M. M.; Liz-Marzán, L. M. Intense Optical Activity from Three-Dimensional Chiral Ordering of Plasmonic Nanoantennas. *Angew. Chem., Int. Ed.* **2011**, *50* (24), 5499−5503.
(24) Majoinen, J.; Hassinen, J.; Haataja, J. S.; Rekola, H. T.; Kontturi, E.; Kostiainen, M. A.; Ras, R. H. A.; Torma, P.; Ikkala, O. Chiral Plasmonics Using Twisting along Cellulose Nanocrystals as a Template for Gold Nanoparticles. *Adv. Mater.* **2016**, *28* (26), 5262−5267.
(25) Palmer, L. C.; Stupp, S. I. Molecular Self-Assembly into One-Dimensional Nanostructures. *Acc. Chem. Res.* **2008**, *41* (12), 1674−1684.
(26) Zubarev, E. R.; Sone, E. D.; Stupp, S. I. The Molecular Basis of Self-Assembly of Dendron-Rod-Coils into One-Dimensional Nanostructures. *Chem. - Eur. J.* **2006**, *12* (28), 7313−7327.
(27) Morrow, S. M.; Bissette, A. J.; Fletcher, S. P. Transmission of Chirality Through Space and Across Length Scales. *Nat. Nanotechnol.* **2017**, *12* (5), 410−419.
(28) Pieraccini, S.; Masiero, S.; Ferrarini, A.; Spada, G. P. Chirality Transfer Across Length-Scales in Nematic Liquid Crystals: Fundamentals and Applications. *Chem. Soc. Rev.* **2011**, *40* (1), 258−271.
(29) Micali, N.; Engelkamp, H.; van Rhee, P. G.; Christianen, P. C. M.; Scolaro, L. M.; Maan, J. C. Selection of Supramolecular Chirality by Application of Rotational and Magnetic Forces. *Nat. Chem.* **2012**, *4* (3), 201−207.
(30) Jones, M. R.; Seeman, N. C.; Mirkin, C. A. Programmable Materials and the Nature of the DNA Bond. *Science* **2015**, *347* (6224), 1260901.
(31) Prins, L. J.; Timmerman, P.; Reinhoudt, D. N. Amplification of Chirality: The "Sergeants and Soldiers" Principle Applied to Dynamic Hydrogen-Bonded Assemblies. *J. Am. Chem. Soc.* **2001**, *123* (42), 10153−10163.
(32) Palmans, A. R. A.; Vekemans, J. A. J. M.; Havinga, E. E.; Meijer, E. W. Sergeants-and-Soldiers Principle in Chiral Columnar Stacks of Disc-Shaped Molecules with C3 Symmetry. *Angew. Chem., Int. Ed. Engl.* **1997**, *36* (23), 2648−2651.
(33) van Gestel, J.; Palmans, A. R. A.; Titulaer, B.; Vekemans, J. A. J. M.; Meijer, E. W. Majority-Rules" Operative in Chiral Columnar Stacks of C3-Symmetrical Molecules. *J. Am. Chem. Soc.* **2005**, *127* (15), 5490−5494.
(34) Smulders, M. M. J.; Stals, P. J. M.; Mes, T.; Paffen, T. F. E.; Schenning, A. P. H. J.; Palmans, A. R. A.; Meijer, E. W. Probing the Limits of the Majority-Rules Principle in a Dynamic Supramolecular Polymer. *J. Am. Chem. Soc.* **2010**, *132* (2), 620−626.
(35) Lee, J. J.; Kim, B. C.; Choi, H. J.; Bae, S.; Araoka, F.; Choi, S. W. Inverse Helical Nanofilament Networks Serving as a Chiral Nanotemplate. *ACS Nano* **2020**, *14* (5), 5243−5250.
(36) Zhang, S. M.; Shi, W. X.; Rong, S. J.; Li, S. Z.; Zhuang, J.; Wang, X. Chirality Evolution from Sub-1 Nanometer Nanowires to the Macroscopic Helical Structure. *J. Am. Chem. Soc.* **2020**, *142* (3), 1375−1381.
(37) Kumar, J.; Thomas, K. G.; Liz-Marzán, L. M. Nanoscale Chirality in Metal and Semiconductor Nanoparticles. *Chem. Commun.* **2016**, *52* (85), 12555−12569.
(38) Govorov, A. O.; Gun'ko, Y. K.; Slocik, J. M.; Gerard, V. A.; Fan, Z. Y.; Naik, R. R. Chiral Nanoparticle Assemblies: Circular Dichroism, Plasmonic Interactions, and Exciton Effects. *J. Mater. Chem.* **2011**, *21* (42), 16806−16818.
(39) Guerrero-Martinez, A.; Alonso-Gomez, J. L.; Auguie, B.; Cid, M. M.; Liz-Marzán, L. M. From Individual to Collective Chirality in Metal Nanoparticles. *Nano Today* **2011**, *6* (4), 381−400.
(40) Gautier, C.; Bürgi, T. Chiral Nanoparticles. In *Chirality at the Nanoscale*; Amabilino, D. B., Ed.; Wiley-VCH Verlag GmbH & Co. KGaA: Weinheim, 2009; pp 67−91.
(41) Green, M. M.; Peterson, N. C.; Sato, T.; Teramoto, A.; Cook, R.; Lifson, S. A Helical Polymer with a Cooperative Response to Chiral Information. *Science* **1995**, *268* (5219), 1860−1866.
(42) Würthner, F.; Chen, Z. J.; Hoeben, F. J. M.; Osswald, P.; You, C. C.; Jonkheijm, P.; von Herrikhuyzen, J.; Schenning, A. P. H. J.; van der Schoot, P. P. A. M.; Meijer, E. W.; Beckers, E. H. A.; Meskers, S. C. J.; Janssen, R. A. J. Supramolecular *p-n*-Heterojunctions by Co-Self-Organization of Oligo(*p*-Phenylene Vinylene) and Perylene Bisimide Dyes. *J. Am. Chem. Soc.* **2004**, *126* (34), 10611−10618.
(43) Jha, S. K.; Cheon, K. S.; Green, M. M.; Selinger, J. V. Chiral Optical Properties of a Helical Polymer Synthesized from Nearly Racemic Chiral Monomers Highly Diluted with Achiral Monomers. *J. Am. Chem. Soc.* **1999**, *121* (8), 1665−1673.
(44) Leigh, T.; Fernandez-Trillo, P. Helical Polymers for Biological and Medical Applications. *Nat. Rev. Chem.* **2020**, *4* (6), 291−310.
(45) Ikai, T.; Okubo, M.; Wada, Y. Helical Assemblies of One-Dimensional Supramolecular Polymers Composed of Helical Macromolecules: Generation of Circularly Polarized Light Using an Infinitesimal Chiral Source. *J. Am. Chem. Soc.* **2020**, *142* (6), 3254−3261.
(46) Bleschke, C.; Schmidt, J.; Kundu, D. S.; Blechert, S.; Thomas, A. A Chiral Microporous Polymer Network as Asymmetric Heterogeneous Organocatalyst. *Adv. Synth. Catal.* **2011**, *353* (17), 3101−3106.
(47) Weissbuch, I.; Leiserowitz, L.; Lahav, M. Structure and Function of Chiral Architectures of Amphiphilic Molecules at the Air/Water Interface. In *Chirality at the Nanoscale*; Amabilino, D. B., Ed.; Wiley-VCH Verlag GmbH & Co. KGaA: Weinheim, 2009; pp 247−270.
(48) Nguyen, M. K.; Kuzyk, A. Reconfigurable Chiral Plasmonics beyond Single Chiral Centers. *ACS Nano* **2019**, *13* (12), 13615−13619.
(49) Hentschel, M.; Schaferling, M.; Duan, X. Y.; Giessen, H.; Liu, N. Chiral Plasmonics. *Sci. Adv.* **2017**, *3* (5), No. e1602735.
(50) Yin, X. H.; Schaferling, M.; Michel, A. K. U.; Tittl, A.; Wuttig, M.; Taubner, T.; Giessen, H. Active Chiral Plasmonics. *Nano Lett.* **2015**, *15* (7), 4255−4260.
(51) Lee, S. J.; Hu, A. G.; Lin, W. B. First Chiral Organometallic Triangle for Asymmetric Catalysis. *J. Am. Chem. Soc.* **2002**, *124* (44), 12948−12949.
(52) Noyori, R. Chiral Metal-Complexes as Discriminating Molecular Catalysts. *Science* **1990**, *248* (4960), 1194−1199.
(53) Quack, M. How Important is Parity Violation for Molecular and Biomolecular Chirality? *Angew. Chem., Int. Ed.* **2002**, *41* (24), 4618−4630.
(54) Hough, L. E.; Jung, H. T.; Kruerke, D.; Heberling, M. S.; Nakata, M.; Jones, C. D.; Chen, D.; Link, D. R.; Zasadzinski, J.; Heppke, G.; Rabe, J. P.; Stocker, W.; Korblova, E.; Walba, D. M.; Glaser, M. A.; Clark, N. A. Helical Nanofilament Phases. *Science* **2009**, *325* (5939), 456−460.
(55) Oda, R.; Huc, I.; Schmutz, M.; Candau, S. J.; MacKintosh, F. C. Tuning Bilayer Twist Using Chiral Counterions. *Nature* **1999**, *399* (6736), 566−569.
(56) Hawbaker, N. A.; Blackmond, D. G. Energy Threshold for Chiral Symmetry Breaking in Molecular Self-Replication. *Nat. Chem.* **2019**, *11* (10), 957−962.

https://doi.org/10.1021/acsnano.1c00527
ACS Nano 2021, 15, 7249−7270

(57) Dozov, I.; Luckhurst, G. R. Setting Things Straight in "The Twist-Bend Nematic: A Case of Mistaken Identity. *Liq. Cryst.* **2020**, *47* (13), 2098−2115.
(58) Samulski, E. T.; Vanakaras, A. G.; Photinos, D. J. The Twist Bend Nematic: A Case of Mistaken Identity. *Liq. Cryst.* **2020**, *47* (13), 2092−2097.
(59) Čopič, M.; Mertelj, A. Q-Tensor Model of Twist-Bend and Splay Nematic Phases. *Phys. Rev. E: Stat. Phys., Plasmas, Fluids, Relat. Interdiscip. Top.* **2020**, *101* (2), 022704.
(60) Walker, R.; Pociecha, D.; Storey, J. M. D.; Gorecka, E.; Imrie, C. T. The Chiral Twist-Bend Nematic Phase (N*(TB)). *Chem. - Eur. J.* **2019**, *25* (58), 13329−13335.
(61) Panov, V. P.; Sreenilayam, S. P.; Panarin, Y. P.; Vij, J. K.; Welch, C. J.; Mehl, G. H. Characterization of the Submicrometer Hierarchy Levels in the Twist-Bend Nematic Phase with Nanometric Helices *via* Photopolymerization. Explanation for the Sign Reversal in the Polar Response. *Nano Lett.* **2017**, *17* (12), 7515−7519.
(62) Gorecka, E.; Vaupotič, N.; Zep, A.; Pociecha, D.; Yoshioka, J.; Yamamoto, J.; Takezoe, H. A Twist-Bend Nematic (N-TB) Phase of Chiral Materials. *Angew. Chem., Int. Ed.* **2015**, *54* (35), 10155−10159.
(63) Borshch, V.; Kim, Y. K.; Xiang, J.; Gao, M.; Jákli, A.; Panov, V. P.; Vij, J. K.; Imrie, C. T.; Tamba, M. G.; Mehl, G. H.; Lavrentovich, O. D. Nematic Twist-Bend Phase with Nanoscale Modulation of Molecular Orientation. *Nat. Commun.* **2013**, *4*, 2635.
(64) Chen, D.; Porada, J. H.; Hooper, J. B.; Klittnick, A.; Shen, Y. Q.; Tuchband, M. R.; Korblova, E.; Bedrov, D.; Walba, D. M.; Glaser, M. A.; Maclennan, J. E.; Clark, N. A. Chiral Heliconical Ground State of Nanoscale Pitch in a Nematic Liquid Crystal of Achiral Molecular Dimers. *Proc. Natl. Acad. Sci. U. S. A.* **2013**, *110* (40), 15931−15936.
(65) Abberley, J. P.; Killah, R.; Walker, R.; Storey, J. M. D.; Imrie, C. T.; Salamonczyk, M.; Zhu, C. H.; Gorecka, E.; Pociecha, D. Heliconical Smectic Phases Formed by Achiral Molecules. *Nat. Commun.* **2018**, *9*, 228.
(66) Hahn, H.; Keith, C.; Lang, H.; Reddy, R. A.; Tschierske, C. First example of a Third-Generation Liquid-Crystalline Carbosilane Dendrimer with Peripheral Bent-Core Mesogenic Units: Understanding of "Dark Conglomerate Phases. *Adv. Mater.* **2006**, *18* (19), 2629−2633.
(67) Hough, L. E.; Spannuth, M.; Nakata, M.; Coleman, D. A.; Jones, C. D.; Dantlgraber, G.; Tschierske, C.; Watanabe, J.; Korblova, E.; Walba, D. M.; Maclennan, J. E.; Glaser, M. A.; Clark, N. A. Chiral Isotropic Liquids from Achiral Molecules. *Science* **2009**, *325* (5939), 452−456.
(68) Sreenilayam, S. P.; Panarin, Y. P.; Vij, J. K.; Panov, V. P.; Lehmann, A.; Poppe, M.; Prehm, M.; Tschierske, C. Spontaneous Helix Formation in Non-Chiral Bent-Core Liquid Crystals with Fast Linear Electro-Optic Effect. *Nat. Commun.* **2016**, *7*, 11369.
(69) Chen, D.; Maclennan, J. E.; Shao, R.; Yoon, D. K.; Wang, H. T.; Korblova, E.; Walba, D. M.; Glaser, M. A.; Clark, N. A. Chirality-Preserving Growth of Helical Filaments in the B4 Phase of Bent-Core Liquid Crystals. *J. Am. Chem. Soc.* **2011**, *133* (32), 12656−12663.
(70) Lewandowski, W.; Vaupotič, N.; Pociecha, D.; Gorecka, E.; Liz-Marzán, L. M. Chirality of Liquid Crystals Formed from Achiral Molecules Revealed by Resonant X-Ray Scattering. *Adv. Mater.* **2020**, *32* (41), 1905591.
(71) Kim, H.; Lee, S.; Shin, T. J.; Korblova, E.; Walba, D. M.; Clark, N. A.; Lee, S. B.; Yoon, D. K. Multistep Hierarchical Self-Assembly of Chiral Nanopore Arrays. *Proc. Natl. Acad. Sci. U. S. A.* **2014**, *111* (40), 14342−14347.
(72) Kim, H.; Ryu, S. H.; Tuchband, M.; Shin, T. J.; Korblova, E.; Walba, D. M.; Clark, N. A.; Yoon, D. K. Structural Transitions and Guest/Host Complexing of Liquid Crystal Helical Nanofilaments Induced by Nanoconfinement. *Sci. Adv.* **2017**, *3* (2), No. e1602102.
(73) Tsai, E.; Richardson, J. M.; Korblova, E.; Nakata, M.; Chen, D.; Shen, Y. Q.; Shao, R. F.; Clark, N. A.; Walba, D. M. A Modulated Helical Nanofilament Phase. *Angew. Chem., Int. Ed.* **2013**, *52* (20), 5254−5257.
(74) Shadpour, S.; Nemati, A.; Salamończyk, M.; Prévôt, M. E.; Liu, J.; Boyd, N. J.; Wilson, M. R.; Zhu, C. H.; Hegmann, E.; Jákli, A. I.; Hegmann, T. Missing Link between Helical Nano- and Microfilaments in B4 Phase Bent-Core Liquid Crystals, and Deciphering which Chiral Center Controls the Filament Handedness. *Small* **2020**, *16* (4), 1905591.
(75) Shadpour, S.; Nemati, A.; Liu, J.; Hegmann, T. Directing the Handedness of Helical Nanofilaments Confined in Nanochannels Using Axially Chiral Binaphthyl Dopants. *ACS Appl. Mater. Interfaces* **2020**, *12* (11), 13456−13463.
(76) Li, L.; Salamończyk, M.; Shadpour, S.; Zhu, C. H.; Jákli, A.; Hegmann, T. An Unusual Type of Polymorphism in a Liquid Crystal. *Nat. Commun.* **2018**, *9*, 714.
(77) Li, L.; Salamończyk, M.; Jákli, A.; Hegmann, T. A Dual Modulated Homochiral Helical Nanofilament Phase with Local Columnar Ordering Formed by Bent Core Liquid Crystals: Effects of Molecular Chirality. *Small* **2016**, *12* (29), 3944−3955.
(78) Alaasar, M.; Prehm, M.; Tschierske, C. Helical Nano-crystallite (HNC) Phases: Chirality Synchronization of Achiral Bent-Core Mesogens in a New Type of Dark Conglomerates. *Chem. - Eur. J.* **2016**, *22* (19), 6583−6597.
(79) Shadpour, S.; Nemati, A.; Boyd, N. J.; Li, L.; Prévôt, M. E.; Wakerlin, S. L.; Vanegas, J. P.; Salamończyk, M.; Hegmann, E.; Zhu, C. H.; Wilson, M. R.; Jákli, A. I.; Hegmann, T. Heliconical-Layered Nanocylinders (HLNCs) - Hierarchical Self-Assembly in a Unique B4 Phase Liquid Crystal Morphology. *Mater. Horiz.* **2019**, *6* (5), 959−968.
(80) Park, W.; Ha, T.; Kim, T. T.; Zep, A.; Ahn, H.; Shin, T. J.; Sim, K. I.; Jung, T. S.; Kim, J. H.; Pociecha, D.; Gorecka, E.; Yoon, D. K. Directed Self-Assembly of a Helical Nanofilament Liquid Crystal Phase for Use as Structural Color Reflectors. *NPG Asia Mater.* **2019**, *11*, 45.
(81) Park, W.; Wolska, J. M.; Pociecha, D.; Gorecka, E.; Yoon, D. K. Direct Visualization of Optical Activity in Chiral Substances Using a Helical Nanofilament (B4) Liquid Crystal Phase. *Adv. Opt. Mater.* **2019**, *7* (23), 1901399.
(82) Sun, J. Y.; Bhushan, B.; Tong, J. Structural Coloration in Nature. *RSC Adv.* **2013**, *3* (35), 14862−14889.
(83) Goodby, J. W.; Slaney, A. J.; Booth, C. J.; Nishiyama, I.; Vuijk, J. D.; Styring, P.; Toyne, K. J. Chirality and Frustration in Ordered Fluids. *Mol. Cryst. Liq. Cryst. Sci. Technol., Sect. A* **1994**, *243*, 231−298.
(84) Taugerbeck, A.; Booth, C. J. Design and Synthesis of Chiral Nematic Liquid Crystals. In *Handbook of Liquid Crystals*; Goodby, J., Collings, P. J., Kato, T., Tschierske, C., Gleeson, H., Raynes, P., Eds.; Wiley-VCH Verlag GmbH & Co. KGaA: Weinheim, 2014; Vol. 3, part III, pp 1−63.
(85) Bloch, K. The Biological Synthesis of Cholesterol. *Vitam. Horm.* **1957**, *15*, 119−150.
(86) DeRosa, S.; Milone, A.; Crispino, A.; Jaklin, A.; DeGiulio, A. Absolute Configuration of 2,6-Dimethylheptyl Sulfate and Its Distribution in Ascidiacea. *J. Nat. Prod.* **1997**, *60* (5), 462−463.
(87) Haddad, A.; Aharoni, H.; Sharon, E.; Shtukenberg, A. G.; Kahr, B.; Efrati, E. Twist Renormalization in Molecular Crystals Driven by Geometric Frustration. *Soft Matter* **2019**, *15* (1), 116−126.
(88) Grason, G. M. Chiral and Achiral Mechanisms of Self-Limiting Assembly of Twisted Bundles. *Soft Matter* **2020**, *16* (4), 1102−1116.
(89) Hall, D. M.; Grason, G. M. How Geometric Frustration Shapes Twisted Fibres, Inside and Out: Competing Morphologies of Chiral Filament Assembly. *Interface Focus* **2017**, *7* (4), 20160140.
(90) Halgren, T. A. Merck Molecular Force Field. 1. Basis, Form, Scope, Parameterization, and Performance of MMFF94. *J. Comput. Chem.* **1996**, *17* (5−6), 490−519.
(91) Halgren, T. A. Merck Molecular Force Field. 2. MMFF94 Van Der Waals and Electrostatic Parameters for Intermolecular Interactions. *J. Comput. Chem.* **1996**, *17* (5−6), 520−552.
(92) Halgren, T. A. Merck Molecular Force Field. 3. Molecular Geometries and Vibrational Frequencies for MMFF94. *J. Comput. Chem.* **1996**, *17* (5−6), 553−586.
(93) Halgren, T. A.; Nachbar, R. B. Merck Molecular Force Field. 4. Conformational Energies and Geometries for MMFF94. *J. Comput. Chem.* **1996**, *17* (5−6), 587−615.

https://doi.org/10.1021/acsnano.1c00527
ACS Nano 2021, 15, 7249−7270

(94) Halgren, T. A. Merck Molecular Force Field. 5. Extension of MMFF94 using Experimental Data, Additional Computational Data, and Empirical Rules. *J. Comput. Chem.* **1996**, *17* (5−6), 616−641.
(95) Becke, A. D. A New Mixing of Hartree-Fock and Local Density-Functional Theories. *J. Chem. Phys.* **1993**, *98* (2), 1372−1377.
(96) Ditchfield, R.; Hehre, W. J.; Pople, J. A. Self-Consistent Molecular-Orbital Methods. IX. Extended Gaussian-Type Basis for Molecular-Orbital Studies of Organic Molecules. *J. Chem. Phys.* **1971**, *54* (2), 724−728.
(97) Thompson, M. P.; Hegmann, T.; Wand, M. D.; Lemieux, R. P. Ferroelectric Liquid Crystal Dopants with a Chiral (*R,R*)-2,3-Difluorooctyloxy Side-Chain: Host Dependence of the Polarization Power. *Liq. Cryst.* **2007**, *34* (8), 987−994.
(98) Zep, A.; Salamończyk, M.; Vaupotič, N.; Pociecha, D.; Gorecka, E. Physical Gels Made of Liquid Crystalline B-4 Phase. *Chem. Commun.* **2013**, *49* (30), 3119−3121.
(99) Shen, D.; Pegenau, A.; Diele, S.; Wirth, I.; Tschierske, C. Molecular Design of Nonchiral Bent-Core Liquid Crystals with Antiferroelectric Properties. *J. Am. Chem. Soc.* **2000**, *122* (8), 1593−1601.
(100) Qi, H.; O'Neil, J.; Hegmann, T. Chirality Transfer in Nematic Liquid Crystals Doped With (S)-Naproxen-Functionalized Gold Nanoclusters: An Induced Circular Dichroism Study. *J. Mater. Chem.* **2008**, *18* (4), 374−380.
(101) Lin, S. C.; Ho, R. M.; Chang, C. Y.; Hsu, C. S. Hierarchical Superstructures with Control of Helicity from the Self-Assembly of Chiral Bent-Core Molecules. *Chem. - Eur. J.* **2012**, *18* (29), 9091−9098.
(102) Castillo-Valles, M.; Cano, M.; Bermejo-Sanz, A.; Gimeno, N.; Ros, M. B. Towards Supramolecular Nanostructured Materials: Control of the Self-Assembly of Ionic Bent-Core Amphiphiles. *J. Mater. Chem. C* **2020**, *8* (6), 1998−2007.
(103) Schneider, C. A.; Rasband, W. S.; Eliceiri, K. W. NIH Image to ImageJ: 25 Years of Image Analysis. *Nat. Methods* **2012**, *9* (7), 671−675.
(104) Chen, D.; Tuchband, M. R.; Horanyi, B.; Korblova, E.; Walba, D. M.; Glaser, M. A.; Maclennan, J. E.; Clark, N. A. Diastereomeric Liquid Crystal Domains at the Mesoscale. *Nat. Commun.* **2015**, *6*, 7763.
(105) Oliveira, I. S.; Lo, M.; Araujo, M. J.; Marques, E. F. Temperature-Responsive Self-Assembled Nanostructures from Lysine-Based Surfactants with High Chain Length Asymmetry: From Tubules and Helical Ribbons to Micelles and Vesicles. *Soft Matter* **2019**, *15* (18), 3700−3711.
(106) Li, Y.; Li, G. T.; Wang, X. Y.; Li, W. N.; Su, Z. X.; Zhang, Y. H.; Ju, Y. Unique Twisted Ribbons Generated by Self-Assembly of Oligo(*p*-Phenylene ethylene) Bearing Dimeric Bile Acid Pendant Groups. *Chem. - Eur. J.* **2009**, *15* (26), 6399−6407.
(107) Wagalgave, S. M.; Padghan, S. D.; Burud, M. D.; Al Kobaisi, M.; La, D. D.; Bhosale, R. S.; Bhosale, S. V.; Bhosale, S. V. Supramolecular Super-Helix Formation *via* Self-Assembly of Naphthalene Diimide Functionalised with Bile Acid Derivatives. *Sci. Rep.* **2019**, *9*, 12825.
(108) Li, C.; Deng, K.; Tang, Z. Y.; Jiang, L. Twisted Metal-Amino Acid Nanobelts: Chirality Transcription from Molecules to Frameworks. *J. Am. Chem. Soc.* **2010**, *132* (23), 8202−8209.
(109) Hayashi, H.; Yamaguchi, J.; Jippo, H.; Hayashi, R.; Aratani, N.; Ohfuchi, M.; Sato, S.; Yamada, H. Experimental and Theoretical Investigations of Surface-Assisted Graphene Nanoribbon Synthesis Featuring Carbon-Fluorine Bond Cleavage. *ACS Nano* **2017**, *11* (6), 6204−6210.
(110) Rizzo, D. J.; Veber, G.; Jiang, J. W.; McCurdy, R.; Cao, T.; Bronner, C.; Chen, T.; Louie, S. G.; Fischer, F. R.; Crommie, M. F. Inducing Metallicity in Graphene Nanoribbons *via* Zero-Mode Superlattices. *Science* **2020**, *369* (6511), 1597−1603.
(111) Cortizo-Lacalle, D.; Mora-Fuentes, J. P.; Strutynski, K.; Saeki, A.; Melle-Franco, M.; Mateo-Alonso, A. Monodisperse N-Doped Graphene Nanoribbons Reaching 7.7 Nanometers in Length. *Angew. Chem., Int. Ed.* **2018**, *57* (3), 703−708.
(112) Reddy, R. A.; Tschierske, C. Bent-Core Liquid Crystals: Polar Order, Superstructural Chirality and Spontaneous Desymmetrisation in Soft Matter Systems. *J. Mater. Chem.* **2006**, *16* (10), 907−961.
(113) Schröder, M. W.; Diele, S.; Pelzl, G.; Dunemann, U.; Kresse, H.; Weissflog, W. Different Nematic Phases and a Switchable SmCP Phase Formed by Homologues of a New Class of Asymmetric Bent-Core Mesogens. *J. Mater. Chem.* **2003**, *13* (8), 1877−1882.
(114) Gorecka, E.; Vaupotič, N.; Zep, A.; Pociecha, D. From Sponges to Nanotubes: A Change of Nanocrystal Morphology for Acute-Angle Bent-Core Molecules. *Angew. Chem., Int. Ed.* **2016**, *55* (40), 12238−12242.
(115) Gray, G. W.; McDonnell, D. G. The Relationship Between Helical Twist Sense, Absolute Configuration and Molecular Structure for Non-Sterol Cholesteric Liquid Crystals. *Mol. Cryst. Liq. Cryst.* **1976**, *34* (9), 211−217.
(116) Person, R. V.; Monde, K.; Humpf, H. U.; Berova, N.; Nakanishi, K. A New Approach in Exciton-Coupled Circular-Dichroism (Eccd) - Insertion of an Auxiliary Stereogenic Center. *Chirality* **1995**, *7* (3), 128−135.
(117) Selinger, R. L. B.; Selinger, J. V.; Malanoski, A. P.; Schnur, J. M. Shape Selection in Chiral Self-Assembly. *Phys. Rev. Lett.* **2004**, *93* (15), 158103.
(118) Ghafouri, R.; Bruinsma, R. Helicoid to Spiral Ribbon Transition. *Phys. Rev. Lett.* **2005**, *94* (13), 138101.
(119) Armon, S.; Aharoni, H.; Moshe, M.; Sharon, E. Shape Selection in Chiral Ribbons: From Seed Pods to Supramolecular Assemblies. *Soft Matter* **2014**, *10* (16), 2733−2740.
(120) Grason, G. M. Perspective: Geometrically Frustrated Assemblies. *J. Chem. Phys.* **2016**, *145* (11), 110901.
(121) Gibaud, T.; Barry, E.; Zakhary, M. J.; Henglin, M.; Ward, A.; Yang, Y. S.; Berciu, C.; Oldenbourg, R.; Hagan, M. F.; Nicastro, D.; Meyer, R. B.; Dogič, Z. Reconfigurable Self-Assembly Through Chiral Control of Interfacial Tension. *Nature* **2012**, *481* (7381), 348−351.
(122) Walba, D. M.; Eshdat, L.; Korblova, E.; Shoemaker, R. K. On the Nature of the B4 Banana Phase: Crystal or Not a Crystal? *Cryst. Growth Des.* **2005**, *5* (6), 2091−2099.
(123) Baginski, M.; Tupikowska, M.; Gonzalez-Rubio, G.; Wojčik, M.; Lewandowski, W. Shaping Liquid Crystals with Gold Nanoparticles: Helical Assemblies with Tunable and Hierarchical Structures *via* Thin-Film Cooperative Interactions. *Adv. Mater.* **2020**, *32* (1), 1904581.
(124) Albano, G.; Pescitelli, G.; Di Bari, L. Chiroptical Properties in Thin Films of π-Conjugated Systems. *Chem. Rev.* **2020**, *120* (18), 10145−10243.
(125) Hexemer, A.; Bras, W.; Glossinger, J.; Schaible, E.; Gann, E.; Kirian, R.; MacDowell, A.; Church, M.; Rude, B.; Padmore, H. A SAXS/WAXS/GISAXS Beamline with Multilayer Monochromator. *J. Phys.: Conf. Ser.* **2010**, *247*, 012007.
(126) Ilavsky, J. Nika: Software for Two-Dimensional Data Reduction. *J. Appl. Crystallogr.* **2012**, *45*, 324−328.

https://doi.org/10.1021/acsnano.1c00527
ACS Nano 2021, 15, 7249−7270